metals

MDPI

Article

Recurrent Neural Networks and Three-Point Bending Test on the Identification of Material Hardening Parameters

Daniel J. Cruz [1,*], Manuel R. Barbosa [1,2], Abel D. Santos [1,2], Rui L. Amaral [1], Jose Cesar de Sa [1,2] and Jose V. Fernandes [3]

[1] Institute of Science and Innovation in Mechanical and Industrial Engineering, R. Dr. Roberto Frias 400, 4200-465 Porto, Portugal; mbarbosa@fe.up.pt (M.R.B); abel@fe.up.pt (A.D.S); ramaral@inegi.up.pt (R.L.A); cesarsa@fe.up.pt (J.C.d.S)

[2] Faculty of Engineering, University of Porto, R. Dr. Roberto Frias s/n, 4200-465 Porto, Portugal

[3] Centre for Mechanical Engineering, Materials and Processes-Advanced Production and Intelligent Systems (ARISE) Associated Laboratory, Department of Mechanical Engineering, University of Coimbra, R. Luís Reis Santos, 3030-788 Coimbra, Portugal; valdemar.fernandes@dem.uc.pt

* Correspondence: dcruz@inegi.up.pt

Abstract: The continuous evolution of metallic alloys in the automotive industry has led to the development of more advanced and flexible constitutive models that attempt to accurately describe the various fundamental properties and behavior of these materials. These models have become increasingly complex, incorporating a larger number of parameters that require an accurate calibration procedure to fit the constitutive parameters with experimental data. In this context, machine learning (ML) methodologies have the potential to advance material constitutive modeling, enhancing the efficiency of the material parameter calibration procedure. Recurrent neural networks (RNNs) stand out among various learning algorithms due to their ability to process sequential data and overcome limitations imposed by nonlinearities and multiple parameters involved in phenomenological models. This study explores the modeling capabilities of long short-term memory (LSTM) structures, a type of RNN, in predicting the hardening behavior of a sheet metal material using the results of a standardized experimental three-point bending test, with the aim of extending this methodology to other experimental tests and constitutive models. Additionally, a variable analysis is performed to select the most important variables for this experimental test and assess the influence of friction, material thickness, and elastic and plastic properties on the accuracy of predictions made by neural networks. The required data for designing and training the network solutions are collected from numerical simulations using finite element methodology (FEM), which are subsequently validated by experiments. The results demonstrate that the proposed LSTM-based approach outperforms traditional identification techniques in predicting the material hardening parameters. This suggests that the developed procedure can be effectively applied to efficiently characterize different materials, especially those extensively used in industrial applications, ranging from mild steels to advanced high-strength steels.

Keywords: machine learning; material parameter identification; three-point bending; recurrent neural networks (RNNs); long short-term memory (LSTM)

Citation: Cruz, D.J.; Barbosa, M.R.; Santos, A.D.; Amaral, R.L.; de Sa, J.C.; Fernandes, J.V. Recurrent Neural Networks and Three-Point Bending Test on the Identification of Material Hardening Parameters. *Metals* **2024**, *14*, 84. https://doi.org/10.3390/met14010084

Academic Editors: Koh-ichi Sugimoto and Xuefeng Tang

Received: 15 December 2023
Revised: 7 January 2024
Accepted: 8 January 2024
Published: 10 January 2024

1. Introduction

In the past few decades, the sheet metal forming industry has faced significant challenges, including the growing complexity of product geometries, the introduction of new advanced materials, and the pressing need to reduce design-production cycles [1]. To address these challenges, there has been a continuous demand for technological advancements and research to reach the so-called "first-time right" solution [2]. One promising solution lies in the integration of machine learning (ML) approaches, which have gained prominence across several industries. The constant evolution of advanced learning algorithms,

driven by the interplay between the availability of large amounts of data (often referred to as "big data") and the exponential growth of computer performance, has revolutionized problem-solving in engineering fields [3,4]. In the context of sheet metal forming, ML algorithms offer a novel approach in studying topics such as [5,6] classification, detection, and prediction of forming defects [7–9]; material modeling and parameter identification [10,11]; process classification [12], design, and optimization [13,14].

The automotive industry is one main driver for the development of theoretical and experimental metal forming technologies [15]. This industry is currently acting to follow the compelling and widespread efforts in addressing environmental concerns of energy savings while also ensuring the demanding safety requirements. To achieve these goals, vehicle manufacturers try to reduce the mass of the products, mainly through the weight of a vehicle's structure, by using lighter and stronger materials, such as advanced high-strength steels (AHSS) [16,17]. Nevertheless, springback is more pronounced in these materials than in conventional steels due to their unique material properties, which lead to additional processing difficulties and costs for industrial applications [18]. To take advantage of the promising properties of AHSS, finite element analysis (FEA) of sheet metal forming processes has become indispensable for predicting and optimizing the product's manufacturing process. In this context, the accuracy of sheet metal forming simulations by FEA is highly affected by the constitutive models chosen to represent the material behavior. This behavior normally includes four independent but interconnected phenomena [19]: (a) the elastic behavior and its influence on springback; (b) the yield criteria; (c) the forming limits; and (d) the hardening model. Regarding the hardening laws, the major developments include the study of the strain rate effects [20], the distortional hardening [21] and the kinematic hardening [22] through the description of the tension–compression stress differential (SD) [23], the Bauschinger effect, the work-hardening stagnation [24], and the permanent softening [25]. Recent advances in this topic have led to the increased complexity of modern constitutive models with additional empirical parameters, making the calibration procedure more difficult and time-consuming, particularly when multiple experimental tests are required [26].

Due to the limitations imposed by nonlinearities and multiple parameters in the constitutive models, several authors have been using ML, including deep learning (DL) networks, as a meta-modeling technique, not only for material parameter inverse identification [27–30] but also for the development of accurate alternative data-driven constitutive models [31,32]. The latter represents a higher level of machine learning integration into constitutive modeling, in which the relationships between stress and strain are learned purely from data without incorporating any prior preconceptions, knowledge, or analytical formulations [33–35]. Huber et al. [36] developed a neural network for identifying material parameters in a finite deformation viscoplasticity model with static recovery. Their study demonstrated that neural networks can identify meaningful material parameter sets, enabling accurate predictions of experimentally observed material behavior, even under complex loading histories. Ktari et al. [37] performed parameter identification for anisotropic thin-walled tubes using the ring hoop tensile test coupled with neural networks. The findings were validated through finite element simulation results. Yao et al. [38] explored a rate-dependent model integrating plasticity and damage. The authors utilized a hybrid approach, merging neural networks with genetic algorithms for parameter identification, focusing on tensile experiments. Morand and Helm [39] proposed multiple parallel-trained multi-layer perceptron (MLP) models to predict hardening model parameters from stress–strain curves. The authors opted for this approach due to the non-uniqueness of the solutions to the problem, concluding that a single MLP model is inadequate for such a complex task.

Recurrent neural networks (RNNs), known for their effectiveness in modelling sequential tasks, can be especially helpful for modeling path-dependent plasticity, as recently demonstrated by different authors [40–44]. In contrast with feed-forward neural networks (FFNNs), RNNs are designed to handle time sequences and effectively incorporate data from previous inputs in future predictions due to extra history-dependent hidden states

presented in the network structure. The architecture of RNNs, being based on recursive operations, is especially suited to model time or order sequences, such as plastic strains and back stresses in physics-based plasticity. In order to model path-dependent plasticity, Mozaffar et al. [44] developed an RNN that uses the time history of the strain field as an input and the corresponding stress field as an output. The authors concluded that the RNN presents superior performance in predicting complex history-dependent plasticity when compared to the conventional FFNNs. In addition to these results, the architecture of RNNs is more complex, and it requires generating high volumes of data for training. Guo et al. [45] created a deep learning model for constitutive parameter identification combining convolutional neural networks (CNNs) to filter input data noise with a long-short term memory (LSTM) neural network, a specific type of RNN. This model identified elastic parameters (Young's modulus and Poisson's ratio) and parameters of an exponential hardening law from uniaxial tensile test results, incorporating strain fields, load history, and geometry information from a specific sample region.

Cruz et al. [46] explored the use of ML algorithms in the form of feed-forward neural networks to model different problems associated with sheet metal processing and material characterization being one problem related to the identification of constitutive parameters. The authors utilized the results of a standard three-point bending test, specifically the punch force–displacement curve, to conduct the mechanical characterization of a metallic sheet material, determining the parameters for the Swift hardening curve given by:

$$\sigma = K(\varepsilon_0 + \varepsilon_p)^n, \tag{1}$$

where σ is the true stress, ε_p is the plastic true strain, and K, ε_0 and n are material parameters known as the strength coefficient, strain offset, and the strain hardening exponent, respectively. The results exhibit strong agreement with simulation and reference models, accurately predicting material parameters.

However, the proposed solution based on FFNNs considers only a few data points of the curves obtained from the available three-point-bending tests to prevent an increase in the network's complexity. Specifically, the authors selected only five representative points from the available punch displacement curves, leading to the underutilization of the information acquired during the test. This under-sampling approach may lead to the oversight of critical features and essential patterns within the curve that can be important to correctly characterize the material behavior. Therefore, considering the results of a three-point bending test in a more comprehensive deep learning approach based on recurrent neural networks can be a major advantage to enhance the accuracy of parameter predictions.

This study aims to advance the use of machine learning techniques for identifying material constitutive parameters, specifically by evaluating the application of RNNs in material parameter identification using a three-point bending test, considering the potential for extending this methodology to other applications and constitutive models. Additionally, the study aims to expand the scope of application by incorporating material parameters that were not previously considered, including the strain offset, ε_0, the elastic modulus, material thickness, and test conditions. The objective is to explore the impact of these factors on the predictions made by neural networks. Accordingly, several sections are defined in this article. Section 2 briefly describes recurrent neural networks, highlighting their major advantages and disadvantages, as well as existing structure variations. Section 3 presents the AHSS materials used in this article along with their experimental characterization of the hardening law using the standard uniaxial tensile test. Additionally, the three-point bending test is introduced, along with a brief study based on numerical results of the influence of fundamental variables on the test result. This analysis forms the basis for selecting the dataset used to train the developed RNNs. Section 4 outlines the implementation of the LSTM models, explaining design choices, the training process, and hyperparameter tuning aimed at optimizing the network's accuracy. Finally, Section 5 analyzes and discusses the results derived from the trained LSTM.

2. Recurrent Neural Networks

Recurrent neural networks (RNNs) are a powerful class of supervised machine learning models specifically designed to handle sequential data and time-series analysis. Unlike feedforward networks (Figure 1a), which propagate information through the network in a unidirectional manner without loops, RNNs (Figure 1b) incorporate cyclic connections, enabling them to process information and memorize dependencies in sequential data by incorporating insights from previous inputs, $\boldsymbol{x}_{0:t-1}$, and not only the current input, $\boldsymbol{x}_t$ [47,48]. This memorization capability enhances the versatility of RNNs, making them essential for various applications, including natural language processing tasks [49,50] and speech recognition applications [51–53].

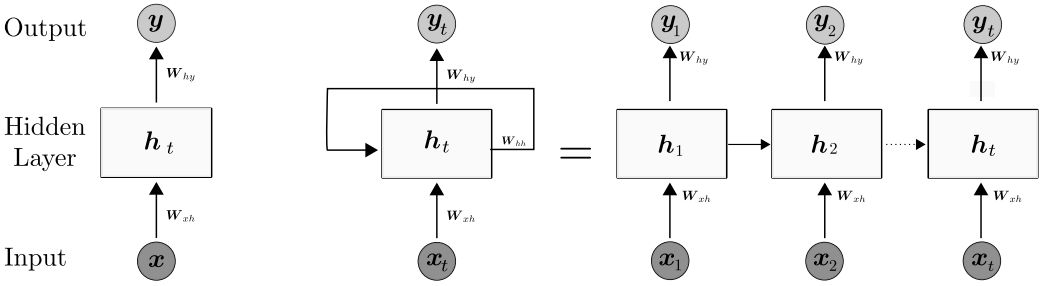

Figure 1. Network structure of a (**a**) feed-forward neural network (FFNN) and (**b**) recurrent neural network (RNN).

RNNs are composed of a hidden layer that can be "unfolded" into several high-dimensional hidden states with non-linear dynamics, forming the network's memory of previous states. This unfolding technique allows RNNs to be trained using backpropagation through time (BPTT), where a consistent set of weights is applied to a layer over different timesteps. At time step t, the hidden state is denoted as $\boldsymbol{h}_t \in \mathbb{R}^{n \times h}$ and the input as $\boldsymbol{x}_t \in \mathbb{R}^{n \times d}$, where n represents the number of samples, d the number of inputs for each sample, and h the number of hidden units. The trained parameters during the BPTT include the weight matrix $\boldsymbol{W}_{xh} \in \mathbb{R}^{d \times h}$, the hidden-state-to-hidden-state matrix $\boldsymbol{W}_{hh} \in \mathbb{R}^{h \times h}$, and the bias parameter $\boldsymbol{b}_h \in \mathbb{R}^{1 \times h}$. These elements form the basic structure of the recurrent neural network. The information from the hidden state and input at each time step undergoes transformation through an activation function ϕ, often a logistic *sigmoid* or *tanh* function, which is crucial for preparing the gradients in the subsequent BPTT algorithm [47].

Using the presented notation, the hidden state, $\boldsymbol{h}_t$, can be defined by Equation (2), while the output variable, $\boldsymbol{y}_t$, can be determined by Equation (3) [54]:

$$\boldsymbol{h}_t = \phi(\boldsymbol{W}_{hh}\boldsymbol{h}_{t-1} + \boldsymbol{W}_{xh}\boldsymbol{x}_t + \boldsymbol{b}_h). \tag{2}$$

$$\boldsymbol{y}_t = \phi(\boldsymbol{W}_{hy}\boldsymbol{h}_t + \boldsymbol{b}_y). \tag{3}$$

Training RNNs presents diverse challenges as the memory formed by recurrent connections can be significantly constrained by the training algorithms employed. Additionally, RNNs face gradient vanishing and exploding problems during the training phase, leading to the network's failure to capture long-term sequential dependencies in data. These problems are characterized by the size of the gradient throughout the training process. When the gradient is too small, it continues to decrease, updating the weight parameters until they become insignificant. When that occurs, the algorithm is no longer learning. On the other hand, exploding gradients happen when the gradient becomes excessively large, leading to an unstable model. In such cases, the model weights grow uncontrollably, compromising the network's stability and undermining effective learning [55].

Long-Short Term Memory

Different modified versions of recurrent neural networks have been proposed to enhance the recall of past data stored in memory. Long short-term memory (LSTM) [49] stands out as one of the most popular and efficient methods for reducing the effects of vanishing and exploding gradients. This approach transforms hidden units into "memory cells" (Figure 2), enabling the storage of additional information beyond the conventional neural network flow in structures known as gated cells. These gates control the flow of data to the hidden neurons and preserve the features extracted from previous times. LSTMs consists of three main components: the output gate, $\boldsymbol{O}_t$, input gate, $\boldsymbol{I}_t$, and forget gate, $\boldsymbol{F}_t$. The input gate regulates the flow of new information into the cell state, while the output gate controls the information that is exposed to the next layers of the network. The forget gate is responsible for controlling the flow of information from the previous time step to the current time step. The computation of these gates is defined by:

$$\boldsymbol{O}_t = \sigma(\boldsymbol{x}_t \boldsymbol{W}_{xo} + \boldsymbol{h}_{t-1} \boldsymbol{W}_{ho} + \boldsymbol{b}_o), \tag{4}$$

$$\boldsymbol{I}_t = \sigma(\boldsymbol{x}_t \boldsymbol{W}_{xi} + \boldsymbol{h}_{t-1} \boldsymbol{W}_{hi} + \boldsymbol{b}_i), \tag{5}$$

$$\boldsymbol{F}_t = \sigma(\boldsymbol{x}_t \boldsymbol{W}_{xf} + \boldsymbol{h}_{t-1} \boldsymbol{W}_{hf} + \boldsymbol{b}_f), \tag{6}$$

where $\boldsymbol{W}_{xo}$, $\boldsymbol{W}_{xi}$, $\boldsymbol{W}_{xf} \in \mathbb{R}^{d \times h}$, and $\boldsymbol{W}_{hi}$, $\boldsymbol{W}_{ho} \boldsymbol{W}_{hf} \in \mathbb{R}^{h \times h}$ are weight matrices, $\boldsymbol{b}_o$, $\boldsymbol{b}_i$, $\boldsymbol{b}_f \in \mathbb{R}^{1 \times h}$ are the biases, and σ represents the sigmoid function responsible for transforming the gate outputs into the range (0, 1). Additionally, an intermediate memory component cell is defined, known as the Cell candidate, $\boldsymbol{c}'_t$, which stores and carries potential new information from the current input ($\boldsymbol{x}_t$) and the previous hidden state ($\boldsymbol{h}_{t-1}$). The candidate memory cell can be determined as:

$$\boldsymbol{c}'_t = tanh(\boldsymbol{x}_t \boldsymbol{W}_{xc} + \boldsymbol{h}_{t-1} \boldsymbol{W}_{hc} + \boldsymbol{b}_c), \tag{7}$$

where $\boldsymbol{W}_{xc}$ and $\boldsymbol{W}_{hc}$ are weight matrices, $\boldsymbol{b}_c$ is the bias term associated with the cell candidate, and *tanh* represents the hyperbolic tangent activation function. This information will be further processed and integrated into the cell state, $\boldsymbol{c}_t$, based on the decisions made by the input gate and the output gate (Equation (8)). The cell state acts as a conveyor belt, allowing information to flow unchanged, thus enabling the network to retain long-term dependencies. Finally, the hidden state, $\boldsymbol{h}_t$ is determined based on the cell state and the output gate (Equation (9)).

$$\boldsymbol{c}_t = \boldsymbol{F}_t \odot \boldsymbol{c}_{t-1} + \boldsymbol{I}_t \odot \boldsymbol{c}'_t. \tag{8}$$

$$\boldsymbol{h}_t = \boldsymbol{O}_t \odot \tanh(\boldsymbol{c}_t). \tag{9}$$

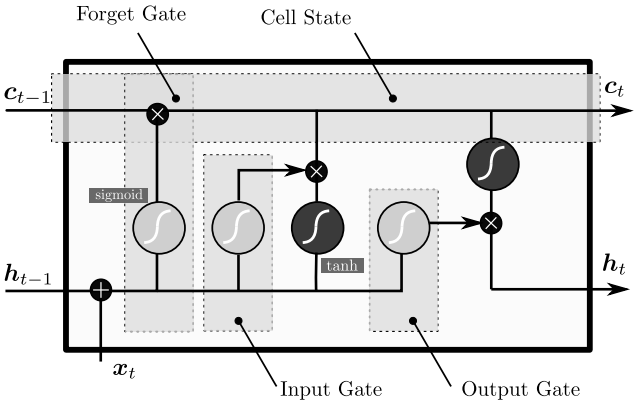

Figure 2. Network structure of an LSTM: $\boldsymbol{x}_t$ represents the input, $\boldsymbol{h}_t$ the hidden state, and $\boldsymbol{c}_t$ the cell state.

3. Materials and Methods

3.1. Materials

The proposed methodology developed in this work was designed to characterize the hardening behavior of steel materials, ranging from mild to advanced high-strength steels, with a nominal thickness of $t_{nominal} = 0.8$ mm. To validate the numerical and experimental developments, three grades of dual-phase (DP) steel sheets were considered: DP500, DP600, and DP780. Table 1 presents the measured thickness values for each material. These measurements were taken using a digital micrometer (Mitutoyo Digimatic) with an accuracy of 2 µm and a step of 0.001 mm, considering 25 different points of measurement. It can be seen that the thickness of DP600 steel exceeds the nominal value of 0.8 mm, with an average thickness of 0.817 mm. On the contrary, the DP500 and DP780 present an average thickness close to the nominal value.

Table 1. Thickness measurements (average, μ and standard deviation, σ) of DP500, DP600, and DP780 sheet metal samples.

	μ [mm]	σ [mm]
DP500	0.802	0.004
DP600	0.817	0.007
DP780	0.801	0.007

Dual-phase steels are a category of AHSS known for their exceptional balance between strength and ductility. This excellent combination arises from the presence of martensite islands within a ferrite matrix, resulting in distinctive mechanical properties that make it suitable for a wide range of applications. The percentage of alloying elements present in the chemical composition of each material is detailed in Table 2.

Table 2. Chemical composition of the DP500, DP600, and DP780 dual-phase steels.

Element (%)	C	Si	Mn	P	S	Cr	Ni	V	Cu	Al	Nb	B	N
DP500	0.079	0.31	0.65	0.003	0.003	0.03	0.03	0.01	0.01	0.038	0.0	0.0003	0.003
DP600	0.089	0.20	0.85	0.014	0.004	0.03	0.03	0.01	0.01	0.046	0.019	0.0003	0.004
DP780	0.138	0.20	1.52	0.011	0.002	0.03	0.03	0.02	0.01	0.038	0.014	0.0002	0.003

Experimental Characterization—Uniaxial Tensile Test

To characterize the hardening behavior of dual-phase steels, experimental uniaxial tensile tests were conducted according to ASTM E8 standards [56] along the rolling direction. The specimens were tested at room temperature using an MTS 810 hydraulic testing machine equipped with a 100 kN load cell. A constant cross speed of 5 mm/min was selected, resulting in an initial strain rate of 10^{-3} s^{-1}. For the acquisition of elongation in the uniform section of the specimen and the corresponding strain evolution, an axial extensometer (Epsilon Technology, ref: 3542-050M-100-HT2, USA) with an initial gauge length of 50 mm was used. The resulting true stress–true strain curves for the tested materials are represented in Figure 3a.

Based on these curves, the hardening behavior was determined using a Swift law represented by Equation (1). The Swift parameters (K, ε_0 and n) were optimized using the Nelder–Mead method [57], also known as the simplex direct search method. This method identifies the minimum mean square error (MSE) between the hardening law prediction and the experimental stress–strain curve obtained from the uniaxial tensile test. Unlike gradient-based methods, the Nelder–Mead method does not require derivatives of the objective function and can handle functions with discontinuities. The identified hardening parameters of the studied materials are summarized in Table 3, and the corresponding hardening evolution curves are plotted in Figure 3b.

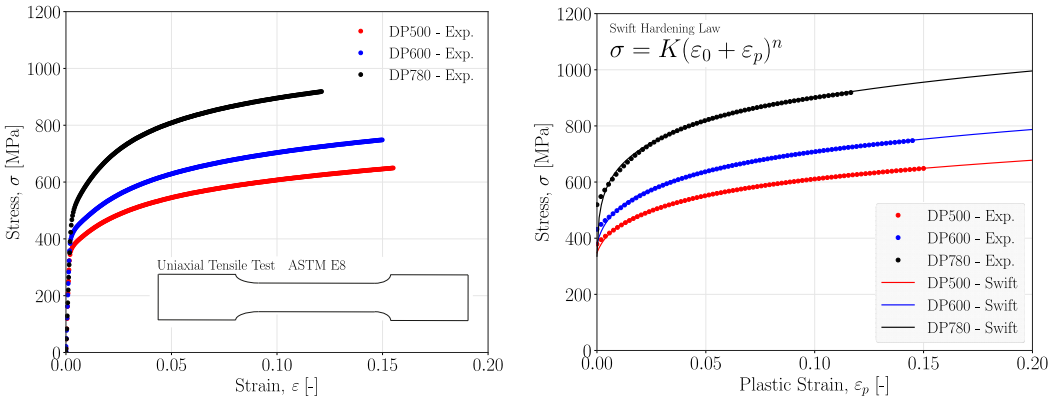

(**a**) (**b**)

Figure 3. Experimental (**a**) true stress–strain curves and (**b**) comparison between the equivalent stress–strain and hardening laws for the different studied materials.

Table 3. Identified parameters for the Swift hardening law based on experimental stress–strain data for dual-phase steels.

	K	ε_0	n
DP500	865.32	0.0026	0.1530
DP600	1011.01	0.0019	0.1563
DP780	1253.72	0.0001	0.1431

3.2. Three-Point Bending Test

The standard ASTM E290 [58] covers several bending tests used to evaluate the behavior of materials when subjected to bending loads under different boundary conditions. The most common is the guided-bend test, which uses a three-point bending setup (Figure 4a) without using a female die. The test is conducted by placing a rectangular specimen symmetrically on the support fixture mounted to the testing machine. Load is applied at the specimen's midpoint until either failure occurs or the predefined angle of bend or maximum angle for the fixture is achieved. The bending angle is determined during the test by projecting lines along the specimen's flat surfaces outside the bend region and measuring their intersecting angle. After completing the bending test, the curved surface of the bend is examined to evaluate the presence of cracks or surface irregularities.

For sheet metal materials, the three-point bending test is widely used to evaluate the springback effect of the tested material. As represented in Figure 4b, the removal of the tools for a punch displacement, y_p, of 20 mm leads to elastic recovery of the material, which results in different bending angles before, α_i, and after, α_f, springback. The springback is entirely intercorrelated with the stress distribution on sheet metal after forming, and its magnitude is related to the ratio between the residual stress and the elastic modulus of the material [59]. It is also influenced by material properties such as strain hardening, elastic property evolution, the presence of Bauschinger effects, elastic and plastic anisotropy, and tribology between contacting surfaces [60].

One of the main advantages of the three-point bending test is its simplicity. In fact, this test does not require any special sample preparation, such as machining and can be easily conducted on a universal tensile testing machine. However, despite its simplicity, challenges arise due to the involvement of axial and transverse forces in the bending deformation [61]. Additionally, factors such as friction, local deformation beneath the contact points [62], and the determination of the stiffness of the testing system [63] can affect the results. Interpreting the raw experimental data, normally represented as punch displacement (y_p) and punch force (F_p), and converting it into a stress–strain ($\sigma - \varepsilon$) response typically involves the use of inverse fitting models [64–66] or analytical approaches [67]. These methods require accurate modeling of the test setup, often involving predetermined

hardening models and iterative optimization loops. This strategy can be time-consuming, particularly when multiple experimental tests are performed. Therefore, the methodology proposed in this article, based on LSTMs, aims to overcome this limitation by determining the stress–strain behavior of a given material using only the results of the three-point bending test. This approach takes advantage of the simplicity of the test, offering an efficient alternative to traditionally inverse and analytical fitting methods for characterizing the material's hardening behavior. The developed LSTM network should consider as input the punch force–displacement curve obtained in a three-point bending test and provide the characteristic parameters of a Swift hardening law (Equation (1)).

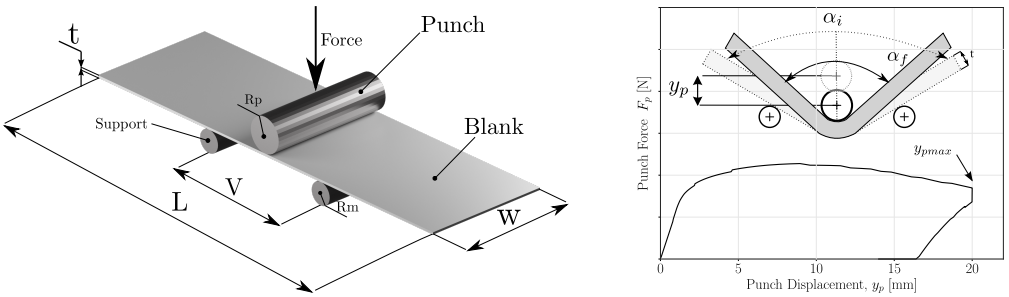

(**a**) (**b**)

Figure 4. Schematic illustration of a (**a**) three-point bending test setup and the main variables: support span (V), support radius (Rm), specimen length (L), specimen width (W), specimen thickness (t), and punch radius (Rp); (**b**) example of a punch force–displacement ($F_p - y_p$) curve of a sheet metal material.

3.2.1. Experimental Details

The experimental three-point bending tests were conducted in an Instron 3900-R universal testing machine equipped with a 1 kN load cell. Detailed information about the test setup and sample geometry can be found in Table 4. Concerning the test conditions, the maximum displacement, y_{pmax} was set at 20 mm, and a crosshead speed of 200 mm/min was employed. During the experimental three-point test, a notable inconsistency is evident between the predicted and expected elastic moduli of the tested materials. This variation is attributed to the stiffness (compliance) of the testing machine, which is influenced by the materials used and the load cell. To address these differences, the determination of the compliance of the testing system, K_s, is carried out, following the methodology outlined in [68]. This process involves applying a load to the specimen supported on a rigid surface. The compliance is then assessed within the linear zone, where the curved region induced by indentation effects disappears [63]. For the particular experimental setup employed in this study, the compliance obtained for the test system was $K_s = 5335$ N/mm.

Table 4. Three-point bending test geometry, test conditions, and sample geometry.

Three-Point Bending Test Geometry			**Test Conditions**	
Punch Radius *Rm* 4 mm	Support Radius *Rp* 6.25 mm	Support Span *V* 50 mm	Max. Displacement y_{pmax} 20 mm	Test Speed *v* 200 mm/min
Sample Geometry				
Lenght *L* 150 mm		Thickness *t* 0.8 mm		Width *W* 45 mm

3.2.2. Finite Element Model

Finite element modeling (FEM) is crucial in the proposed methodology, acting as a tool to build the dataset needed to develop and train the LSTMs. The three-point bending test

can be defined as a plane strain problem in which the blank width is much larger than the blank thickness. Due to the symmetry of this test, only half of the real experimental setup was considered in the 2D finite element model. The numerical model was developed using ABAQUS with implicit analysis (ABAQUS/Standard) [69]. Punch and die were modeled as fully analytical rigid surfaces, and the blank material was modeled with an elastoplastic behavior using the Swift law for the hardening curve. The sheet blank was discretized using 819 deformable four-node solid elements (CPE4R type from the ABAQUS Library) and nine layers through the thickness. For mesh discretization, a regular spacing was employed both in the thickness and length directions. Coulomb friction was incorporated into the model with a value of 0.1 [70]. Using this numerical model, a punch force–displacement curve and the variation in the bending angle during the test are obtained. The corresponding curves for the studied dual-phase steels (DP500, DP600, and DP780) are represented in Figure 5. For each material, an experimental curve is also included. The parameters presented in Table 3 were considered to model the plastic behavior of the dual-phase steels. The elastic behavior was modeled using Young's modulus, E, of 210 GPa and a Poisson's ratio, ν, of 0.3. The numerical results are consistent with the experiments, validating the proposed FEA model.

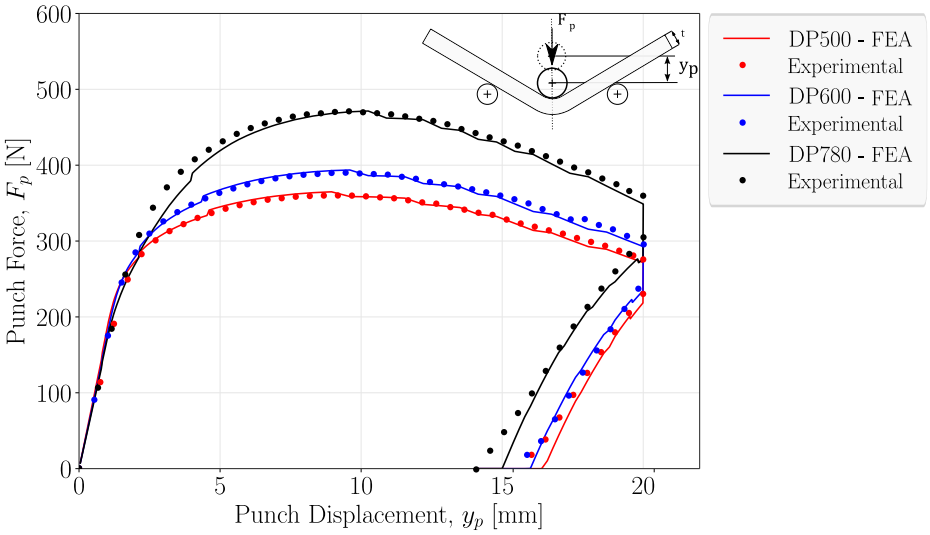

Figure 5. Three-point bending force–displacement curves ($F_p - y_p$) for the studied dual-phase steels (DP500, DP600, DP780) obtained by finite element analysis, with comparison to experimental results.

3.2.3. Analysis of Fundamental Variables

As highlighted in Section 1, the three-point bending test was used in a previous study [46] in which feed-forward artificial neural networks were integrated with the test results to predict the parameters of a well-known hardening curve, the Swift law (Equation (1)). However, the analysis was restricted to only two variables (K and n) in order to reduce the dataset size and the complexity of the developed artificial neural network (ANN). In order to broaden the applicability of the developed methodology, in this section, the influence of different variables of interest on the results of the three-point bending test will be evaluated. These variables are associated with material properties, such as elasto-plastic behavior and material thickness, as well as test conditions. In the analysis, primarily conducted using numerical results obtained through FEA, a key focus is placed on assessing the impact of small variations in these variables on the results. This preliminary study represents a fundamental step in the decision-making process, enabling the informed selection of inputs and outputs for the ML methodology.

Effect of Swift Hardening Law Parameters

The first variable under analysis is the strain offset parameter, ε_0, of the swift hardening law. To analyze the influence of this parameter on the punch force–displacement results,

DP500 steel will be used as an illustrative example. Using the numerical model presented in Section 3.2.2 and the hardening parameters outlined in Table 3, different numerical simulations were conducted. These simulations considered values of the parameter ε_0 ranging from 0.0001 to 0.01 while maintaining the parameters K and n constant at 865.32 and 0.1530, respectively. The resulting punch force–displacement curves (y_p-F_p) for each ε_0 value are depicted in Figure 6a. As evident in this figure, ε_0 has a significant influence on the bending curve, particularly in the transition between the elastic and plastic zones.

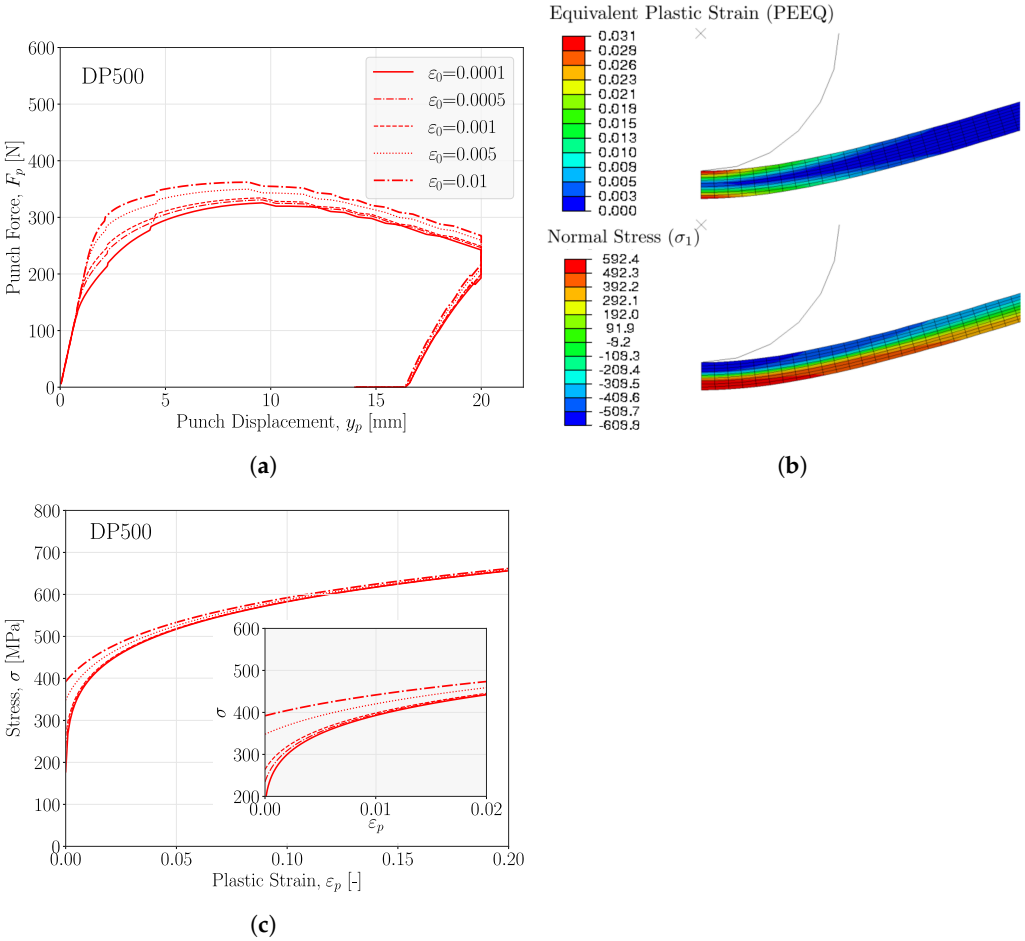

Figure 6. Influence of the ε_0 parameter on the three-point bending: (**a**) force–displacement curve ($y_p - F_p$) (**b**) equivalent plastic strain (PEEQ) and principal stress fields for a $y_p = 7$ mm, and (**c**) the influence of ε_0 on the material plastic curve ($\sigma - \varepsilon_p$).

Analyzing the stress–strain curves ($\sigma - \varepsilon_p$) illustrated in Figure 6c, it becomes evident that the parameter ε_0 exerts a significant influence on the obtained stress value, σ, particularly at low plastic strain values ($\varepsilon_p < 0.10$). In contrast, as the strain values increase, the curves tend to converge, indicating a reduced impact of ε_0 on the plastic behavior. In fact, the levels of strain values obtained in a three-point bending test are low, as illustrated in Figure 6b. This figure displays both the equivalent plastic strain (PEEQ) and stress fields in the thickness of the material on the three-point bending test for a punch displacement, y_p of 5 mm. For this instance, the maximum value of equivalent plastic strain is approximately 0.03. Therefore, upon analyzing Figure 6c at this specific value of plastic strain, it becomes evident that the corresponding stress value varies depending on the ε_0 considered. Additionally, the yield stress, σ_y, for $\varepsilon_p = 0$, varies with different ε_0 values, resulting in distinct behaviors during the elasto-plastic transition of the bending force–displacement curves. Considering the observed influence of ε_0 on the bending curve, especially in the transition between the elastic and plastic zones (Figure 6a), it becomes evident that the

developed model should incorporate not only the parameters K and n but also the variable ε_0 in order to achieve a more accurate prediction of the material's hardening behavior.

Effect of Young's Modulus

As mentioned in Section 3.1, the methodology developed in this study is specifically designed for steel materials, with a particular focus on advanced high-strength steels (AHSS). The elastic properties can vary across different grades of steels, with Young's Modulus typically falling between 200 and 210 GPa. In addition, Young's modulus can vary with the orientation relative to the rolling direction of the material, as indicated in the study by Deng et al. [71]. To assess the influence of variations in Young's modulus on the three-point bending curves, a sensitivity analysis was conducted using DP500 and DP780 materials. Numerical simulations were carried out, adjusting Young's modulus within the range of 190 and 220 GPa while keeping plastic components constant, as specified in Table 3. The resulting curves for DP500 and DP780 are presented in Figure 7a. Despite uncertainties in elastic material characteristics, variations in Young's Modulus were observed to have a minimal impact on punch force–displacement curves in three-point bending tests. As expected, the curves closely coincide throughout the test, diverging only in the elastic regions. Although the modulus of elasticity may not exert a substantial influence on the curves derived from the three-point test, a detailed understanding of the material's elastic properties is crucial to prevent errors when determining the material's plastic parameters. Hence, alongside determining the material's hardening parameters, the methodology should also conduct a preliminary check to confirm the material's classification as steel.

Applying the Euler–Bernoulli theory in a plane strain analysis and treating the initial flat sheet as a beam, the deflection of the sheet, δ, in the elastic region in response to the punch force, can be determined as:

$$\delta = \frac{F_p V^3}{48 E' I} \tag{10}$$

where I is the moment of inertia of the specimen, and V is the support span (see Figure 4). The modulus of elasticity, E', is slightly different from the uniaxial Young's modulus, E, and can be expressed as follows:

$$E' = \frac{E}{1-\nu^2}, \tag{11}$$

where ν is the Poisson's ratio. Considering the sheet deflection equal to the punch displacement, $\delta = y_p$, the material Young's modulus can be calculated by:

$$E = \frac{F_p V^3}{(48 y_p I)(1-\nu^2)}. \tag{12}$$

This equation enables the calculation of the three-point bending modulus using the punch force–displacement curve. Using the three-point bending results presented in Figure 7a for the DP500 and DP780 materials and applying Equation (12), the elastic bending modulus is shown in Figure 7b for different punch displacement values lower than $y_p = 1$ mm. It is evident that the obtained modulus, derived from the theoretical approach, tends to converge toward a constant value that is approximately close to the expected value. This analytical approach will be the basis of comparison for validating the predictions generated by the ML approach developed.

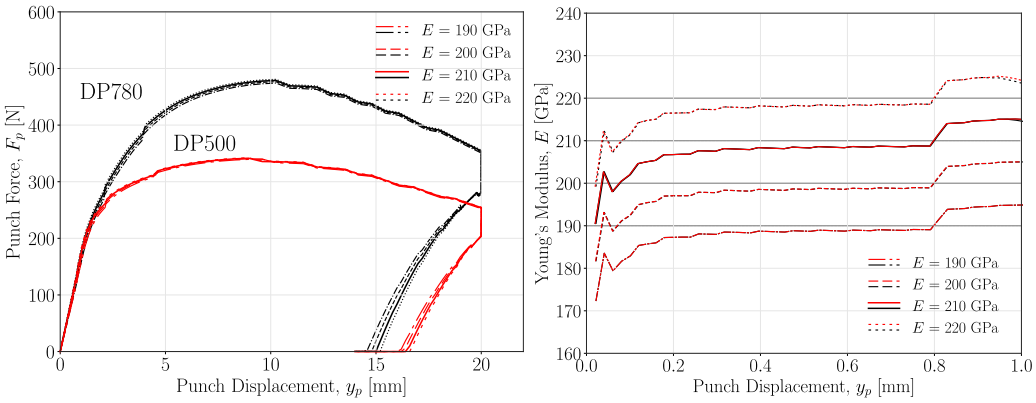

(**a**) (**b**)

Figure 7. Representation of (**a**) the influence of Young's modulus variations on DP500 and DP780 three-point bending curves and (**b**) the corresponding elastic bending modulus (Equation (12)).

Effect of Material Thickness

An important source of variability to consider is associated with material thickness. In the context of sheet metal materials, variations in thickness are common due to the manufacturing process, resulting in differences in thickness from coil to coil and also from head to tail [72]. Therefore, it is important to evaluate the impact of these small thickness variations on the outcomes of the three-point bending test. To address this question, a sensitivity analysis was conducted using DP600 material as a representative case, aiming to evaluate the influence of variations in material thickness on the three-point bending $F_p - y_p$ curve. Numerical simulations were carried out for different thicknesses within a range of ± 0.1 mm from the nominal value, resulting in material thicknesses between 0.7 and 0.9 mm, respectively. The corresponding curves for each case are presented in Figure 8a. The figure illustrates that even minor fluctuations in material thickness can significantly impact the force–displacement curve. Therefore, it is crucial to consider material thickness to prevent the potential impact of even minor variations on the predictions made by the developed neural networks.

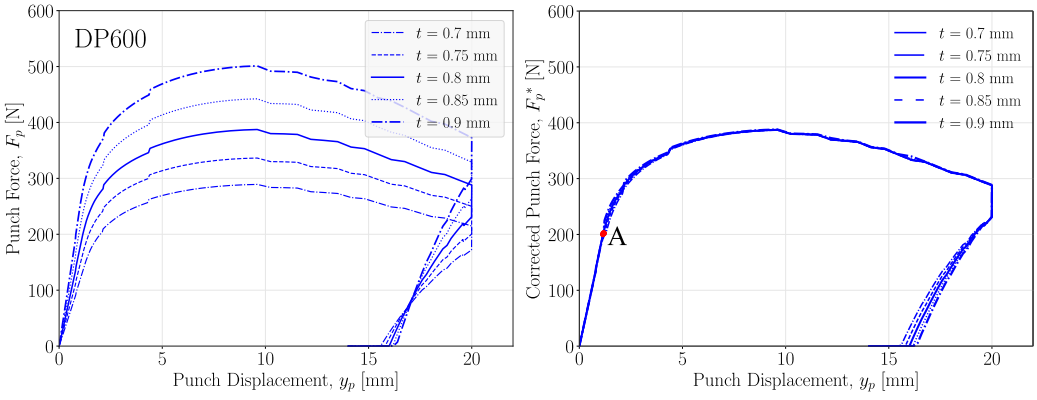

(**a**) (**b**)

Figure 8. Influence of material thickness in three-point bending curves in the case of DP600: (**a**) original punch force–displacement curves ($F_p - y_p$); (**b**) corrected punch force–displacement curves ($F_p^* - y_p$).

Analyzing the stress distribution on the normal section of a sheet bent profile and considering that the material is strain-hardening according to a Swift law, the equilibrium equation is deduced using the moment M (see Figure 9), as follows [73]:

$$M = \int_{-\frac{t}{2}}^{\frac{t}{2}} \sigma_1 \, y \, dy. \tag{13}$$

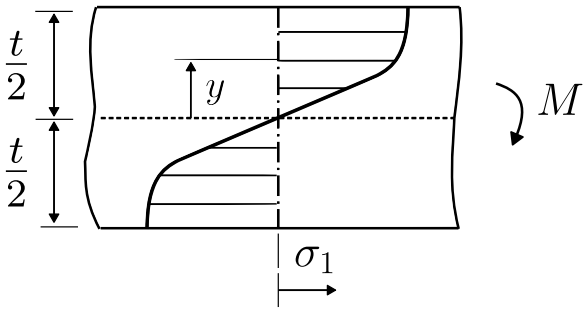

Figure 9. Stress distribution on a normal section in bending, considering a strain-hardening material.

The entire section is assumed to behave under elastoplastic deformation, and stress, σ_1, at some distance, y, from the middle surface is given by:

$$\sigma_1 = K(\varepsilon_0 + \varepsilon_1)^n = K\left(\varepsilon_0 + \frac{y}{\rho}\right)^n, \tag{14}$$

where ρ is the radius of curvature of the bending sheet. This equation reduces to the linear elastic model considering $n = 1$, $K = E'$, and $\varepsilon_0 = 0$. Therefore, the equilibrium equation can be written as:

$$M = 2K\int_0^{\frac{t}{2}}\left(\varepsilon_0 + \frac{y}{\rho}\right)^n y\,dy = 2K\rho^{-n}\left[\frac{t^{n+2}}{2^{n+2}(n+2)} - \frac{\varepsilon_0 t^{n+1}}{2^{n+1}(n+1)}\right]. \tag{15}$$

Simplifying the terms, the following equation can be defined for bending a non-linear material:

$$\frac{M}{I_n} = 2K\rho^{-n}, \tag{16}$$

where I_n represents the second moment of area for a unit width of sheet, which is given by:

$$I_n = \frac{t^{n+2} - 2\varepsilon_0 t^{n+1}}{2^{n+2}(n+2)(n+1)}. \tag{17}$$

Based on these considerations, it is possible to normalize the force–displacement curves for different material thicknesses relative to the nominal material thickness (t_{nom}) using a new variable, the corrected punch force (F_p^*), which can be calculated as follows:

$$F_p^* = F_p \cdot \left(\frac{I_n^t}{I_n^{t_{nom}}}\right), \tag{18}$$

where I_n^t and $I_n^{t_{nom}}$ represent the second moment of area for the case of thickness t (different from t_{nom}) and nominal thickness, respectively. Therefore, it can be concluded that the normalized curve depends not only on the material thickness, t, but also on the hardening parameters n and ε_0.

The normalized curves for each thickness of the DP600 material are represented in Figure 8b. The normalization procedure considers two different conditions. For points in the elastic regime, up to the point represented by letter A, the second moment of area was calculated considering the linear elastic model with $n = 1$ and $\varepsilon_0 = 0$. On the other hand, for points in the plastic regime (i.e., points after the point A, see Figure 8b), the parameters n and ε_0 from Table 3 were considered. This normalization procedure brings the normalized curves for each thickness into closer alignment with the nominal curve ($t_{nom} = 0.8$ mm) both in the elastic and plastic zones. This presents a significant advantage in this study, allowing the methodology to be applied to materials with slight deviations from the nominal thickness. Additionally, it reduces the number of virtual cases needed for numerical simulation, as the generated dataset will only consider material thicknesses of 0.8 mm.

Effect of Friction

Friction is an inherent aspect of the three-point bending test, with forces emerging at two locations: at the contact points between the sheet and punch, and between the sheet and the supports. Friction is characterized by Coulomb's friction force model, where the friction force is directly proportional to the normal force and a friction coefficient. While it is improbable for the friction coefficient to remain constant throughout the process, for simplicity, an average coefficient, μ, is assumed [74]. Nevertheless, accurately determining the friction coefficient for the three-point bending test poses challenges due to factors such as the machining quality of the specimen surface and the structure of the supporter during the test [75]. To analyze the impact of the friction coefficient on the test results, a sensitivity analysis was numerically conducted using DP steels (DP500, DP600, and DP780). Different Coulomb friction coefficients, μ, ranging from 0.02 to 0.4, were considered to characterize the friction between the sheet and the tools. The elastic behavior was defined by a constant Young's modulus, E, of 210 GPa and a Poisson coefficient, ν, of 0.3. Plastic behavior was described using the Swift parameters presented in Table 3. The results for the studied materials, depicted in Figure 10, highlight a significant impact of the friction coefficient on the obtained punch force values during the test. As expected, a higher friction coefficient corresponds to a higher punch force for a fixed displacement value. An interesting point to analyze is related to the moment when the punch ceases its downward movement and initiates an upward motion—denoted as point A in Figure 10a.

At this point, the friction force at the points where the sheet touches the supports changes sign, and as is visible for all materials, the difference between the force between points A and B is strongly influenced by the coefficient of friction present. Based on the work of [74], the friction coefficient can be estimated as:

$$\mu = \frac{\Delta F sin(90 - \alpha)}{2F_m sin(\alpha)}, \tag{19}$$

where ΔF represents the drop in punch force between points A and B, F_m is the mean value between F_A and F_B, and α represents half of the bending angle at position A. Using as an example the DP500 with an expected friction value of $\mu = 0.04$, the bending angle in point A is $\alpha = 83.83°$, F_m is equal to 232 N, and ΔF of 199 N. These values lead to an estimated friction value of $\mu = 0.046$, which closely matches the expected value.

To establish the potential range of friction coefficients within the available experimental setup, three-point bending tests were conducted using dual-phase steels. Two lubrication conditions were tested: dry and abundant application of lubricant to both the supports and sheet metal, using Quaker 6130 lubricant. The experimental details, as outlined in Section 3.2.1, were taken into account. The results for both lubrication conditions are illustrated in Figure 10d for DP500, DP600, and DP780. As visible, the presence of lubricant for the experimental setup considered does not significantly change the force values. Additionally, the drop of force for a punch displacement, y_p of 20 mm is approximately the same for both conditions and is coherent across the three materials. Therefore, a constant friction coefficient can be assumed. Comparing these values with the reference curve obtained numerically, it can be observed that the friction coefficient for this experimental test is near 0.1 regarding the lubrication conditions employed. Consequently, the friction coefficient will not be considered as a variable of interest to be predicted by the developed ML model.

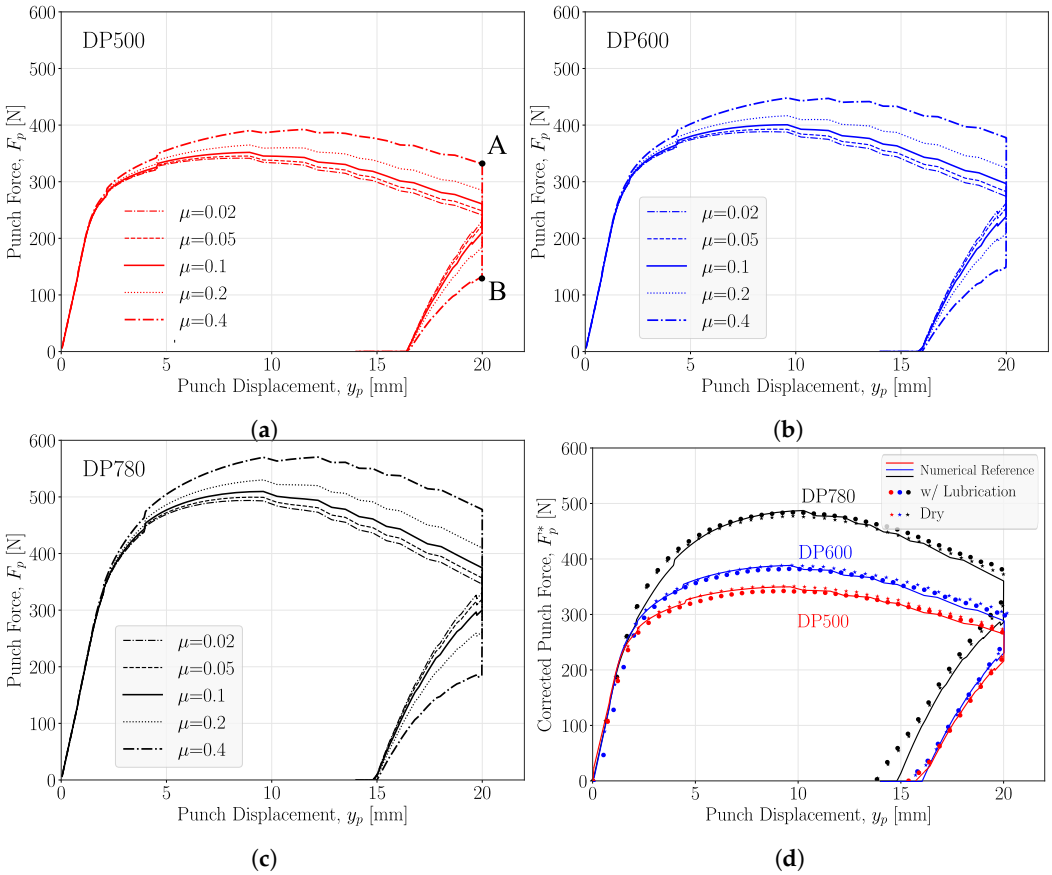

Figure 10. Influence of the friction coefficient, μ, on the force–displacement curves of the three-point bending for (**a**) DP500, (**b**) DP600, and (**c**) DP780; (**d**) influence of friction conditions (dry and abundant lubrication) on the experimental three-point bending test results; points A and B in (**a**) correspond to the moments when the punch ceases its downward movement and initiates an upward motion.

3.3. Proposed Methodology

Based on the preceding analysis, this study proposes a machine learning framework based on long short-term memory networks to predict both elastic and plastic parameters of sheet metal materials based on experimental three-point bending test curves. The methodology employed is schematically depicted in Figure 11. Initially, an experimental force–displacement curve is obtained through a standardized three-point bending test, following the test conditions outlined in Section 3.2.1. The acquired experimental data are then processed, and the force is normalized using Equation (18). This correction ensures that the force values become independent of small variations in material thickness in relation to a nominal thickness. Subsequently, a first ML algorithm (*ML model—elasticity*), based on LSTM networks, is deployed to evaluate the elastic segment of the force–displacement curve, ultimately determining the associated elastic parameters, i.e., Young's modulus (E). As mentioned earlier, this methodology is specifically tailored for steel materials, where the hardening behavior is well-described by a Swift law. In the event that the calculated modulus falls within the range of 190 to 220 GPa, a secondary ML algorithm comes into play. This secondary algorithm then extracts the corresponding hardening parameters, providing a comprehensive mechanical characterization of the material. However, if the calculated Young's modulus does not fall within this specified range, the algorithm stops, bypassing the second ML model. In such cases, the algorithm only provides the pertinent elastic parameters and alerts the user that the material is not steel, and therefore, the plastic components will not be calculated. Accordingly, this methodology ensures a systematic and robust approach to mechanical characterization, particularly tailored to steel materials and their hardening characteristics. The outlined steps guarantee a compre-

hensive understanding of the material's elastic and plastic mechanical behavior, facilitating accurate predictions.

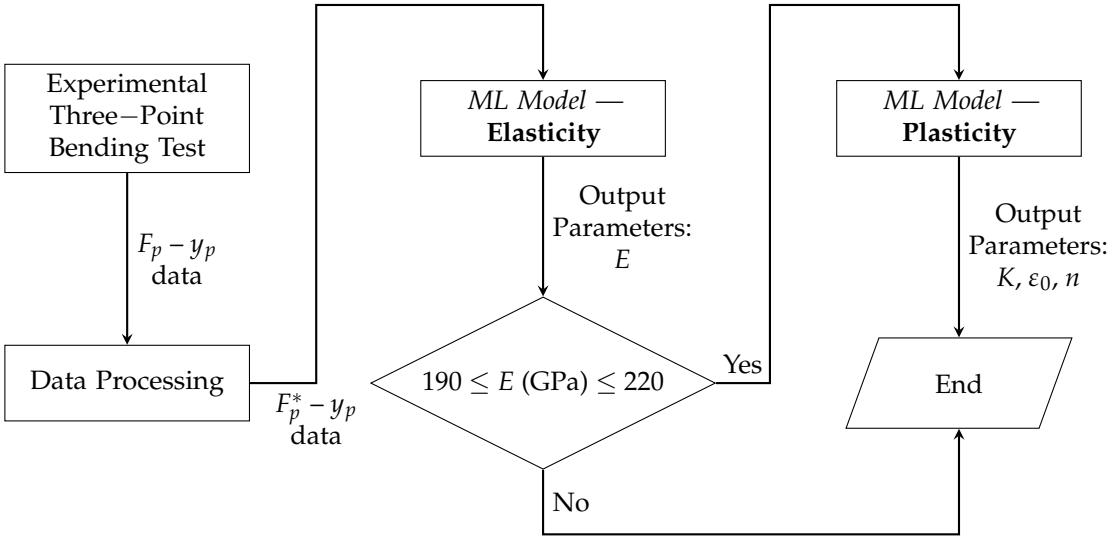

Figure 11. Flowchart illustrating the proposed methodology for predicting elastic and plastic parameters of sheet metal materials using experimental three-point bending test curves and RNNs.

The data required to train the ML models was obtained using the numerical model presented in Section 3.2.2. Python scripts were developed to automatically create and modify the finite element model, enabling the consideration of different material parameters. These scripts were also employed to submit the analyses. To extract results from each of the preceding numerical simulations, an additional Python script was developed. This script is responsible for extracting fundamental data for the development of LSTMs, including punch displacement, punch force, bending angle, and material parameters.

Two distinct datasets were considered, one for training the *ML model—elasticity* (Section 4.1) and the other for training the *ML model—plasticity* (Section 4.2). The key characteristics of both datasets are summarized in Table 5. For the ML model that predicts Young's modulus of the tested material, 20 different Young's modulus values were numerically considered, equally spaced within $E = [70, 250]$ GPa. For each value, three different sets of hardening parameters (K, n and ε_0) were randomly chosen within the intervals specified in the table, resulting in 60 distinct virtual materials. The second dataset was created to have sufficient data to train the ML model responsible for predicting the hardening parameters of steels. Consequently, the elastic parameters were fixed at $E = 210$ GPa and $\nu = 0.3$. The plastic parameters were considered to be variable, with the combinations illustrated in Figure 12, resulting in a total of 637 cases. Thirteen values of K uniformly distributed within $K = [400, 1600]$ were selected, and seven values of the n parameter were selected uniformly distributed in the range $n = [0.05, 0.35]$. For the parameter ε_0, seven cases were considered in the range $\varepsilon_0 = [0.0001, 0.01]$. The combination of these three parameters covers the characterization of the hardening behavior of different types of steel materials, ranging from mild steels to advanced high-strength steels.

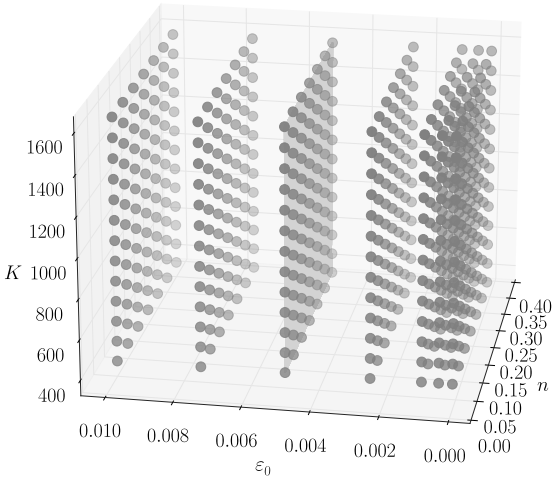

Figure 12. Combinations of Swift hardening parameters (K, n, ε_0) selected to generate the dataset for training the *ML model—plasticity* consist of 13 values for the K variable ranging between 400 and 1600 with increments of 100, 7 values for the n variable ranging between 0.05 and 0.35 with increments of 0.05, and 7 values for ε_0 {0.0001, 0.0005, 0.001, 0.0025, 0.005, 0.0075, 0.01}.

Table 5. Elastic properties and Swift law hardening parameters considered to develop the ML models.

Properties		ML Model—Elasticity	ML Model—Plasticity
Elastic Modulus	E	50–240 GPa	210 GPa
Poisson Coefficient	ν	0.3	0.3
Swift Parameter	K	400–1600	400–1600
	ε_0	0.0001–0.01	0.0001–0.01
	n	0.05–0.35	0.05–0.35

4. Long Short-Term Memory Implementation

As mentioned in Section 2, long short-term memory (LSTM) networks are designed to address various sequence-related problems. In this study, LSTMs are applied to solve a "sequence-to-one" problem, wherein the model processes an input sequence and generates a single output at the end of the analysis of the complete sequence. The first model focuses on predicting the Young's modulus parameter (*ML model—elasticity*), while the second is dedicated to predicting plastic parameters K, n, and ε_0 (*ML model—plasticity*). The sequential nature of the data obtained from the three-point bending test can be effectively managed by the LSTM architecture, allowing the model to capture patterns and dependencies within the sequential punch force–displacement curve. The following sections explore the implementation of LSTM-based models for both ML models, offering insights into the training process.

4.1. Implementation of ML Model—Elasticity

The data needed to train the model were divided into three separate data sets: training, validation, and testing. This division ensures that the model learns from a substantial part of the data (training dataset), validates its performance on cases not seen during training (validation dataset), and finally, evaluates its generalization (testing dataset). Proportions of 70%, 15%, and 15% were considered, resulting in 42 cases for training, 9 for validation, and 9 for testing. Figure 13 shows examples of punch force–displacement curves selected from the original dataset. The selection is restricted to cases with Young's moduli of 100 and 220 GPa. In the figure, a color scheme is employed for clarity: grey denotes cases from the training dataset, black curves represent cases from the validation dataset, and red curves correspond to cases from the testing dataset.

The main objective of this ML model is to determine the Young's modulus of the tested material. Therefore, it is reasonable to consider only the data points from the initial phase of the test, where the relationship between force and displacement follows a linear pattern. Specifically, for each curve derived from numerical simulation, originally comprising a total of 500 points, 20 points were selected within the punch displacement range of $y_p = 0$ mm to $y_p = 2$ mm. It is worth noting that, in some instances, these selected points may include data from the plastic component, as visually demonstrated in Figure 13.

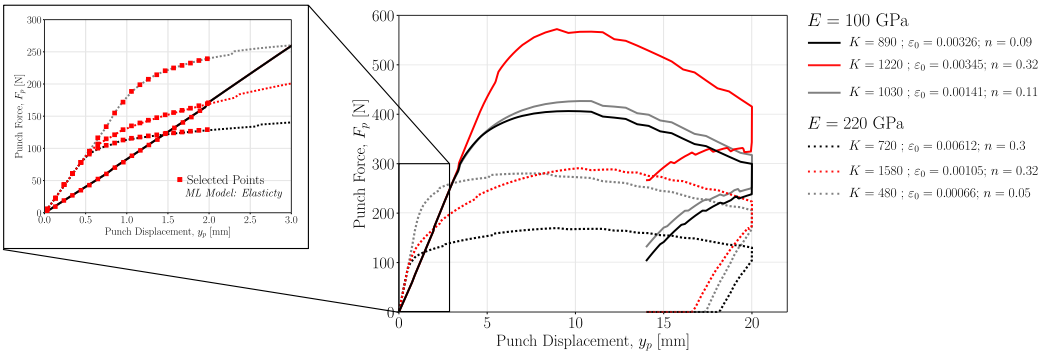

Figure 13. Punch force–displacement curves for cases in the training (grey), validation (black), and testing (red) datasets, illustrating selected points for ML development within the $y_p = 0$ mm to $y_p = 2$ mm range.

The development of the ML model and the subsequent training process were implemented using Python code, making use of the robust deep learning library Keras [76] for LSTM networks. In configuring the LSTM model, a crucial parameter to account for is the number of hidden units in the LSTM layer. This value corresponds to the dimensionality of the output space, i.e., the size of the hidden state at a given time step, $\boldsymbol{h}_t$ in Equation (9) and determines the capacity of the model to capture patterns in the sequential data. For this preliminary ML model developed, as the relationship between variables is essentially linear, only five hidden units were considered in the LSTM layer. After the LSTM layer, a dense layer was incorporated to aggregate the output of each hidden unit into a single output, representing the value of Young's modulus.

Normalization of data is a fundamental preprocessing step in the development of ML models. This practice stabilizes and speeds up the training process, ensuring that the model learns efficiently without being affected by varying scales in the input and output features. In this context, both input and output variables were normalized to a standardized range between -1 and 1. The training process employed the Adam optimization algorithm to minimize the mean square error (MSE) loss function in the validation dataset. The Adam optimization algorithm is an adaptive learning rate optimization algorithm with exponential decay. In this case, an initial learning rate of 0.1 is applied and undergoes a reduction of 0.96 every 100 epochs. The model was trained for a total of 2500 epochs, and the best-performing epoch on the validation set was selected.

The training curves depicted in Figure 14a demonstrate the convergence of both the training and validation errors throughout 2500 epochs. Both error curves converge to a minimized error value, presenting an MSE in the order of 1×10^{-4}. This value was determined with the input and output normalized. Such convergence is indicative of the model's robust learning without signs of overfitting.

More information on the model's performance can be found in Figure 14b, illustrating the coefficient of determination, R-squared (R2), for the prediction of Young's modulus. Notably, the coefficient R2 is approximately one across all three datasets, indicating a high level of accuracy in the predictions. In the most challenging case, denoted by the letter A, the obtained relative error is 2.5%, falling within the testing dataset. For this specific case, the expected Young's modulus is 220 GPa, and the ML model predicted 214 GPa, which is

an acceptable deviation. Despite a difference of 6 GPa, this material is still classified as steel, as the obtained Young's modulus falls within the admissible range ($190 \leq E(\text{GPa}) \leq 220$).

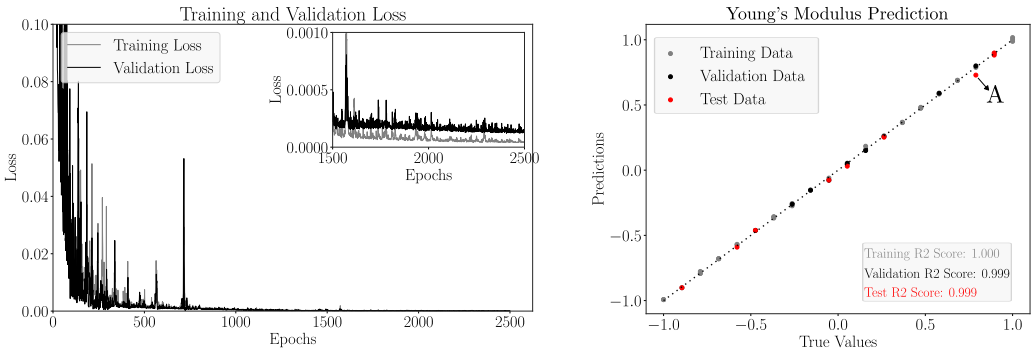

(**a**) (**b**)

Figure 14. Training and performance evaluation figures illustrating (**a**) the convergence of error curves and (**b**) coefficient of determination (R2) in the training, validation, and testing datasets.

4.2. Implementation of ML Model—Plasticity

For the identification of the parameters of a Swift hardening law, an alternative LSTM variant was explored—namely, the Bidirectional LSTM. This choice is justified by the availability of the complete sequence of curves ($F_p - y_p$) during the predicting phase. This particular recurrent neural network architecture processes input data bidirectionally, considering both forward and backward directions. Unlike simpler LSTM models that focus only on past context, bidirectional LSTMs cover both past and future context, allowing them to capture more detailed patterns in sequential data. In the context of a three-point bending test, the punch force–displacement sequence is processed by the bidirectional LSTM in two passes: one from the beginning of the test ($y_p = 0$ mm) to the end (forward pass) and another from the end to the beginning (backward pass). The outputs from both passes are then combined to provide a comprehensive representation of the input sequence.

Considering the dataset presented in Figure 12, comprising 637 cases, three distinct datasets were created. Following the approach of the previous ML model, the data were randomly divided into training, validation, and testing sets with a distribution of 70%, 15%, and 15%, respectively. This division resulted in 446 cases for the training dataset, along with 95 cases each for the validation and testing datasets, as shown in Figure 15. As mentioned earlier, each curve in the dataset is structured with a total of 500 discrete points for punch force and displacement. To streamline the data and minimize time spent during the training process, each curve is uniformly sampled to include a total of 100 points. The chosen number of points reflects a balance between the expressive capacity of the curve without loss of relevant information and the associated computational costs.

The hyperparameter tuning process is crucial for optimizing the performance of any ML model. In this context, hyperparameters are parameters whose values cannot be learned from the data. Fine-tuning these hyperparameters is essential to optimize the model's overall effectiveness and generalization capabilities of the algorithm. Two different hyperparameters were considered for this model: the number of units of the bidirectional LSTM and the decay steps. The range of variability for these hyperparameters is shown in Table 6, along with the fixed training parameters. A Bayesian optimization strategy [77] was applied to systematically explore and identify the optimal hyperparameter configuration. Multiple runs were considered, and the best performance was achieved with a total of 40 hidden units in the bidirectional LSTM and 3670 decay steps. Although each run was trained for 50,000 epochs, the final model prioritizes the network weights associated with the lowest error in the validation dataset.

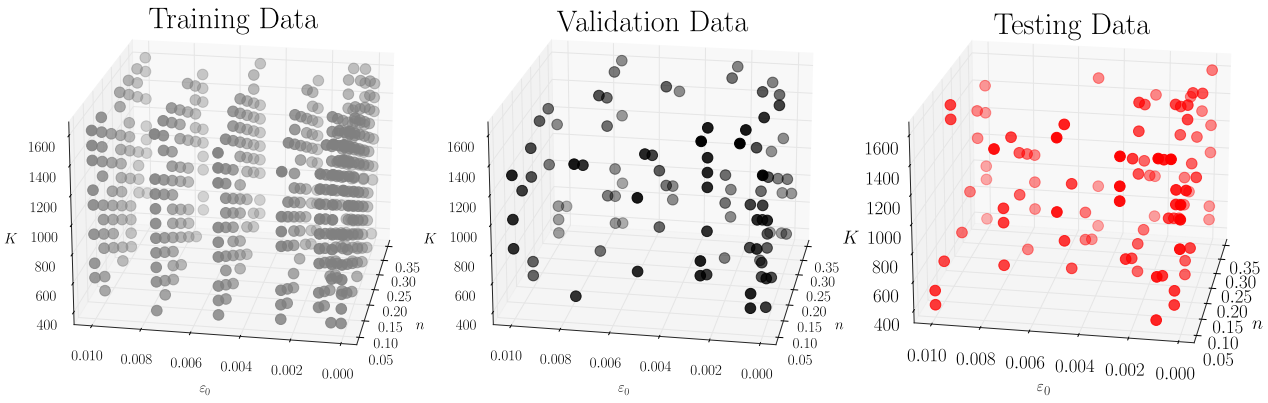

(**a**) (**b**) (**c**)

Figure 15. Distribution of cases in (**a**) training dataset (grey color), (**b**) validation dataset (black color), and (**c**) testing dataset (red color), resulting from the random division of the complete dataset (637 cases).

The results for the best model are presented in Figure 16. This figure shows the coefficient of determination, R-squared (R2), for each variable (K, ε_0 and n) split in each dataset (training, validation, and testing). Both the true values and the predictions are represented as normalized values. Similar to the previous model, both inputs and outputs have been normalized within the range $[-1, 1]$. By analyzing the results, it can be observed that, overall, the R-squared values are close to 1 for all variables across the three datasets. As anticipated, the model demonstrates higher performance on the training dataset with an R^2 of 1 compared to the validation and testing datasets, which present lower values. When comparing the prediction of the three variables, it is noticeable that the parameter ε_0 has the lowest R-squared value in the testing dataset (Figure 16f), registering 0.987. This could be related to the limited number of cases in the original dataset, as only seven values for ε_0 were considered within the range of [0.01 to 0.0001]. Improving the prediction performance may involve generating more data distributed across the specified range. The variable n also shows some values outside the expected range, particularly in the testing dataset (Figure 16i).

In each dataset, three different cases are highlighted, denoted by the letter W. For instance, in the training dataset (Figure 16a,d,g), cases W_K, W_{ε_0}, and W_n represent the instances with the worst performance for the variables K, ε_0, and n, respectively. These instances are characterized by higher absolute errors between the predicted values and the true values. It is noteworthy that for the validation dataset, the worst cases for n and ε_0 correspond to the same instance. These specific cases will be further examined in the next section to conduct a more detailed analysis of the model's performance.

Table 6. Summary of training parameters

Training Parameters	
Parameter	**Value/Range**
Number of Units	[10, 80]
Optimizer	Adams
Learning Rate	0.1
Decay Steps	[500, 5000]
Batch Size	64
Decay Rate	0.96
Epochs	50,000
Hyperparameter Tuner	Bayesian Optimization

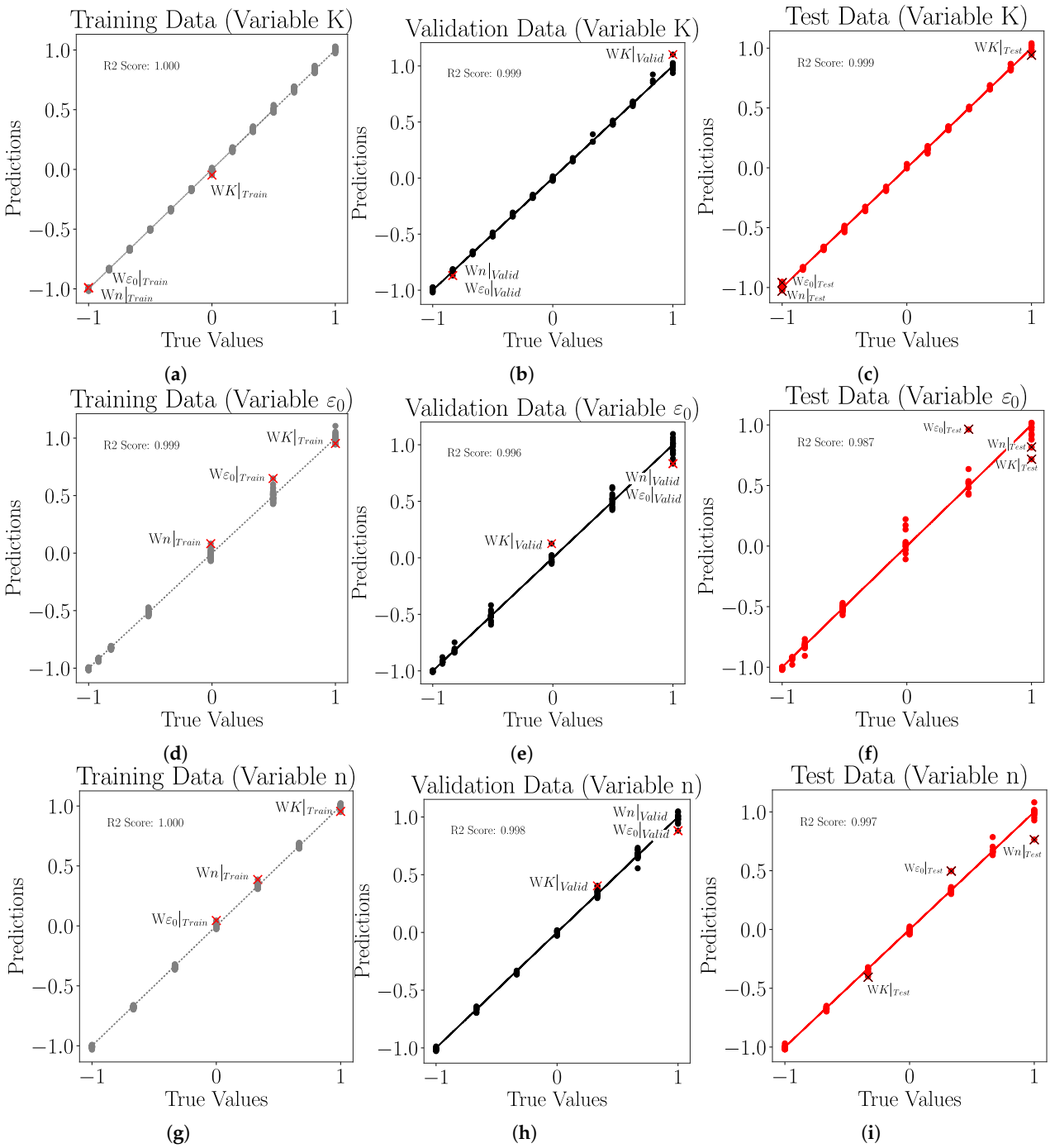

Figure 16. Coefficient of determination (R-squared) for each dataset (training, validation, and testing) across (**a**–**c**) variable K, (**d**–**f**) variable ε_0, and (**g**–**i**) variable n.

5. Results

5.1. Results for the ML Model—Elasticity

Based on the best model presented in Section 4.2, this section provides additional results with three new virtual materials to complement the analysis of the predictive capabilities of the *ML model—elasticity*. For that, the three-point bending test was numerically simulated for the three new virtual materials, denoted as *VM1*, *VM2*, *VM3*, with Young modulus values of 75, 215, and 22 GPa, respectively. These elastic parameter values were not included in the original dataset used for developing the ML model, which means that the trained model was not exposed to such values during its training and testing phase. For each virtual material (*VM1*, *VM2*, *VM3*), the plastic parameters (K, ε_0, and n) were randomly

selected from the admissible range presented in Table 5. The corresponding values for each virtual material are summarized in Table 7. Based on these elastic and plastic parameters, the three-point punch force–displacement curves represented in Figure 17 were obtained by FEA. For each curve, twenty points up to a punch displacement of $y_p = 20$ mm were considered as input for the trained ML model and are also represented in the figure. The Young's modulus predicted by the trained LSTM is summarized in Table 7. The results demonstrate good accuracy, as the predicted values closely match the true values, with a relative error consistently below 3% for the additional virtual materials. This high level of accuracy is indicative of the model's robust generalization capability, performing well not only on materials of the original dataset but also on new randomly created materials. Additionally, it can be concluded that the prediction is independent of the plastic parameters of the material since these values were randomly selected both in the training dataset and in these additional cases. Even though, for some materials, the 20 points chosen contain points outside the elastic regime, the ML model can effectively predict the respective modulus of elasticity of the material. Following the intended approach of using the ML presented in Figure 11, in this case, only the virtual material *VM2* would be considered as steel and advance to the next stage.

Table 7. Plastic parameters (K, ε_0, n) randomly chosen for virtual materials (*VM1*, *VM2*, *VM3*) and their corresponding Young's modulus (E) predictions by the ML model, along with a comparison to the true values.

	Swift Parameters			**Young's Modulus (E)**		
Material	K	ε_0	n	**True Values (GPa)**	**Prediction (GPa)**	**Relative Error**
VM1	1020	0.007	0.23	75.00	75.91	1.21%
VM2	10111	0.0019	0.16	215.00	215.07	0.03%
VM3	1150	0.0032	0.32	225.00	221.68	1.48%

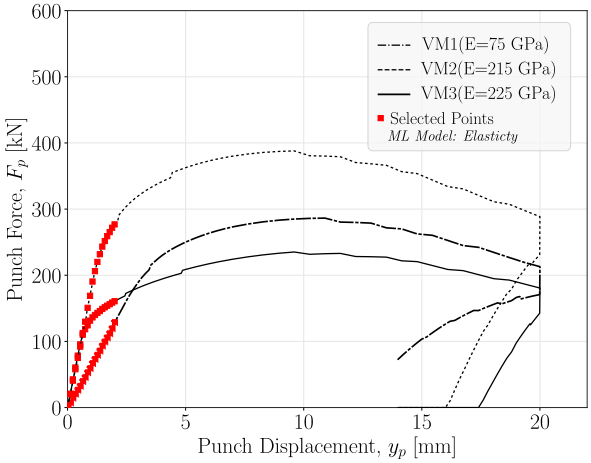

Figure 17. Three-point bending punch force–displacement curves obtained by FEA for virtual materials *VM1*, *VM2*, and *VM3* with Young's modulus (E) values of 75, 215, and 225 GPa, respectively.

5.2. Results for the ML Model—Plasticity

Based on the best model presented in Section 4.2, this section provides additional results to complement the analysis of the predicted capabilities of the *ML model—plasticity*. Figure 18 illustrates the overall relationship between the three targets (K, ε_0, and n) and the obtained predictions for the entire dataset (637 cases) used in the development of this model. In each graph, points marked with a blue star represent the predictions obtained by the developed model, and the circles represent the true/expected values. In this representation, the Swift parameters (K, ε_0, and n) are shown in non-normalized values. It is visible that the

majority of cases exhibit a close alignment between predictions and true values, particularly evident in the training dataset. However, in some instances within the validation and testing datasets, there is a slight deviation between predictions and true values.

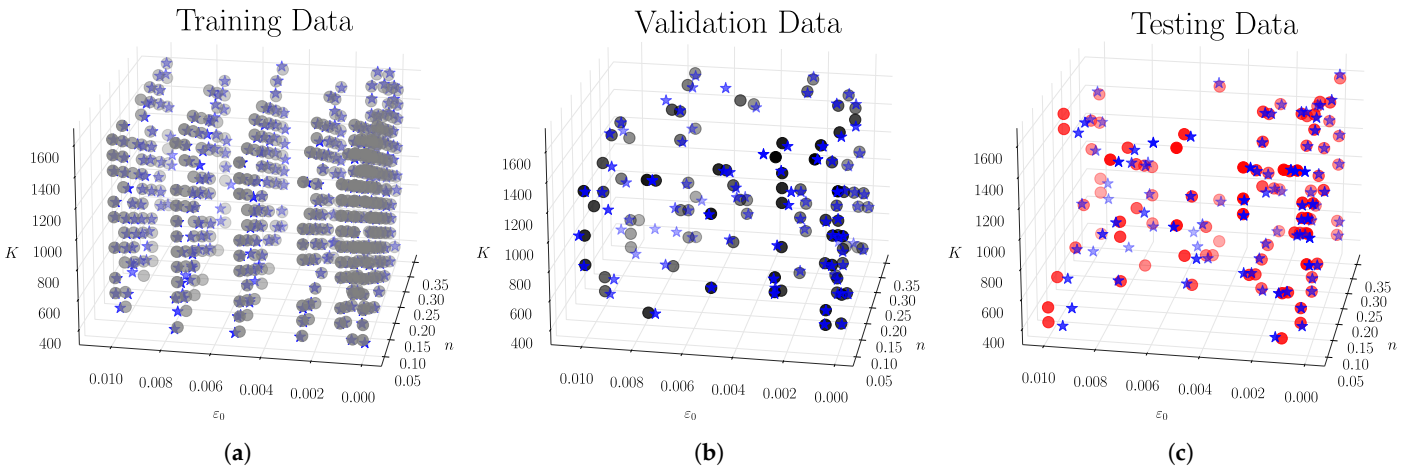

Figure 18. Schematic representation of the comparison between the target (circles) and the prediction (blue stars) for (**a**) the training dataset (grey color), (**b**) the validation dataset (black color) and (**c**) the testing dataset (red color).

In order to quantify the worst cases and assess the influence of the prediction on the resultant Swift curve, the instances labeled as *W* introduced in Figure 16 were analyzed and are represented in Figure 19. The corresponding true stress–strain ($\sigma - \varepsilon_p$) curve for each worst case, within a true strain range of $\varepsilon_p = [0, 0.2]$, is presented in Figure 19a–c for the training, validation, and testing datasets, respectively. Additionally, an example of a case with an accurate prediction result is shown for each dataset ($Best|_{Train}$, $Best|_{Valid}$, and $Best|_{Test}$). For each case, two different stress–strain curves are presented: one obtained considering the true parameter values (solid line), and the other using the parameters predicted by the developed ML model (dashed/dotted lines). To better quantify the errors between the stress values calculated using Swift parameters predicted by the ML model and the true values, Figure 19d–f display the true stress error, $\Delta\sigma$, for the cases belonging to the training, validation, and testing datasets, respectively. The true stress error is determined by the difference between the stress calculated by the ML model and the target value of stress ($\Delta\sigma = \sigma_{LSTM} - \sigma_{target}$) for each value of plastic strain, ε_p.

Analysis of the best cases in the three datasets ($Best|_{Train}$, $Best|_{Valid}$, and $Best|_{Test}$) indicates that the predicted curves closely align with the target curve for the considered range of plastic strain, exhibiting a stress error lower than approximately 5 MPa in all datasets. This error value can be representative of the majority of the total number of cases, as depicted in Figure 20. This figure includes both the histogram of the maximum absolute stress error, $|\Delta\sigma|_{\max}$, (Figure 20a) and the corresponding quartile analysis (Figure 20b). The maximum absolute stress error, $|\Delta\sigma|_{\max}$, corresponds, for each case, to the maximum absolute difference in stress values determined between a plastic strain, ε_p, of 0 and 0.2. The quartile analysis shows that 75% of the total number of cases (75th percentile Q3) present a maximum absolute stress error lower than 5 MPa. Additionally, 97% of the cases present a maximum absolute stress error lower than 9.3 MPa, which in this context can be considered completely acceptable. As evident from the analysis, 24 outliers have been identified, with the histogram revealing that these cases are primarily from the validation and testing datasets. Despite the existence of these outliers, they just represent 3% of all cases, with the maximum absolute stress error never exceeding 30 MPa. This result suggests that the proposed ML model, based on LSTMs, is capable of accurately determining the Swift parameters for the majority of cases in the dataset. Additionally, the chosen LSTM structure—specifically, one bidirectional LSTM layer with 40 hidden units—seems to be

adequate for capturing the patterns in the sequential data and establishing correlations between these patterns and the corresponding hardening parameters.

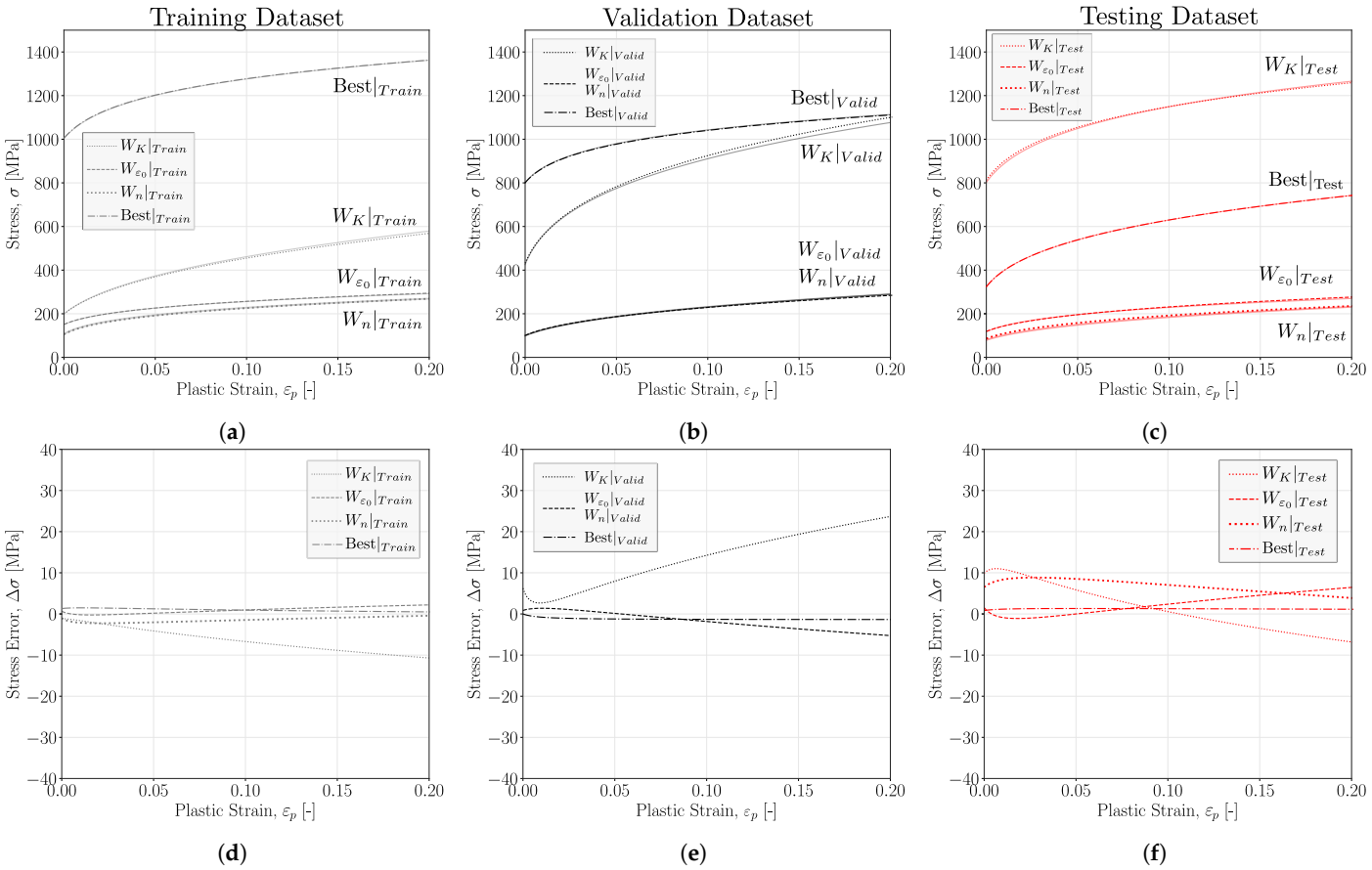

Figure 19. Comparison of predicted (dashed/dotted line) and expected (solid line) true stress–strain curves ($\sigma - \varepsilon_p$) for cases W_K, W_{ε_0}, and W_n for the training (**a**), validation (**b**) and testing (**c**) datasets and respective true stress errors, $\Delta\sigma$, for the training (**d**), validation (**e**) and testing (**f**) datasets; $Best|_{Train}$, $Best|_{Valid}$ and $Best|_{Test}Best|_{Train}$ are examples of cases with an accurate prediction result.

The worst cases (W_K, W_n, and W_{ε_0}) across the three datasets reveal potential outliers in the predictions. In the training dataset, the highest stress error, Figure 19a,d, occurs for the case $W_K|_{Train}$ at a plastic strain value of $\varepsilon_p = 0.2$, presenting a maximum absolute stress error of approximately 10 MPa. Therefore, as indicated in Figure 20b, this case is considered an outlier. The expected K value for this case is 1000, and the predicted value is 971.56, resulting in a relative error below 3%. On the other hand, the worst cases, $W_n|_{Train}$ and $W\varepsilon 0|_{Train}$, can be considered accurate results, as the maximum absolute stress error is below 5 MPa.

For the validation dataset, as illustrated in Figure 19b,e, the worst case is again the one that considers the maximum absolute error in the prediction of the K parameter, $W_K|_{Valid}$. The expected K value for this case is 1600, and the predicted value is 1661.31, resulting in a relative error in the prediction of approximately 3%. This difference leads to a maximum absolute stress error value of 23 MPa for a plastic strain value of $\varepsilon_p = 0.2$. Consequently, as illustrated in Figure 20, this case stands out as the most extreme outlier in the prediction, meaning that all the other cases exhibit superior performance. As mentioned earlier, for the validation dataset, the worst cases, $W_n|_{Valid}$ and $W_{\varepsilon_0}|_{Valid}$, are the same, meaning they have the same hardening parameters. Similar to the training dataset, this case can be considered a good result, as the stress error falls within the acceptable range of ± 5 MPa.

Finally, for the testing dataset, as depicted in Figure 19c,f, the maximum stress errors for the cases $W_K|_{Test}$, $W_n|_{Test}$ and $W_{\varepsilon_0}|_{Test}$ are similar and closer to 10 MPa. Once again,

the parameter K contributes the most to the increase in the stress error, which, in this case, represents an outlier, as represented in Figure 20b. From this analysis, it can be concluded that the K parameter has the greatest influence on the maximum stress error obtained. It should, therefore, be the parameter with the lowest prediction error in order to minimize the stress errors. An analysis of the performance graphs presented in Figure 16 confirms that this variable is, in fact, the best performer in this methodology, with an R2 very close to unity.

Although the prediction of the parameters ε_0 and n is not as accurate as for the parameter K, it can be concluded that the influence of the prediction errors obtained for these parameters does not have a notable impact on the final stress–strain curve. The worst cases for these two variables (W_{ε_0} and W_n) exhibit errors of less than 10 MPa for the three datasets, suggesting absolute stress errors similar to the majority of the total cases.

An important aspect to highlight is the value of stress for a plastic deformation of zero, i.e., the yield stress, obtained by the ML approach. This value is generally well determined for the cases analyzed, with errors below 10 MPa. Assuming that the outliers presented represent the worst cases, it can be concluded that the proposed ML model demonstrates a high degree of accuracy in predicting the stress–strain relationship, with maximum errors never exceeding 30 MPa.

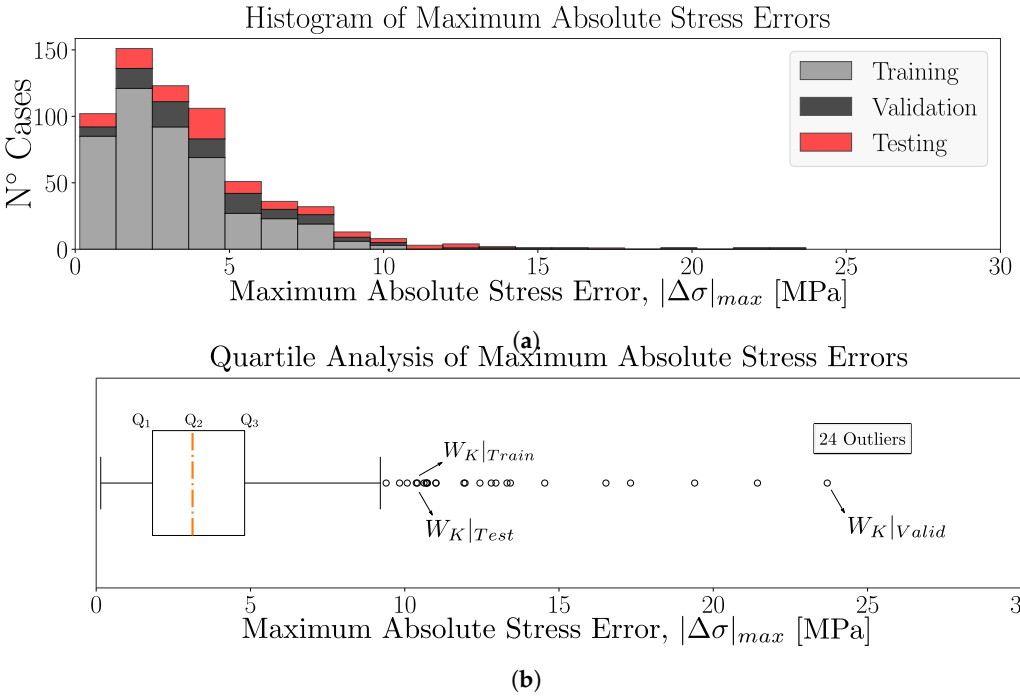

Figure 20. Representation of (**a**) histogram of maximum absolute stress errors $|\Delta\sigma|_{max}$ and (**b**) respective quartile analysis.

Results for Materials with Thickness Variations

As stated in Section 3.3, the proposed methodology should be prepared to be applied to materials with thicknesses within a range $t = 0.8 \pm 0.1$ mm. Therefore, in Section 3.2.3, a new approach was used to transform the sequence of punch force, F_p, into a corrected punch force, F_p^*. This variable standardizes the force values in relation to the nominal thickness, t_{nom}, as given in Equation (18), using not only the material thickness but also the material hardening parameters (n and ε_0). However, these two variables are among the main outputs to be predicted by the developed machine-learning model. Consequently, before conducting the three-point bending tests, they are unknown. To address this issue, a compromise solution is to consider average values for both variables. Given that the admissible parameter space for n and ε_0 is $[0.05, 0.35]$ and $[0.0001, 0.01]$, respectively, the following analysis will consider the use of arbitrarily intermediate values of $n = 0.15$ and

$\varepsilon_0 = 0.001$. To validate this simplification, two new virtual materials, denoted as *VM4* and *VM5*, were considered, and their parameters are presented in Table 8. Both materials have a K parameter of 600 but have distinct values for the remaining parameters. Specifically, *VM4* presents the lower parameter combination, with $n = 0.05$ and $\varepsilon_0 = 0.0001$, while *VM5* represents the higher parameter combination, with $n = 0.35$ and $\varepsilon_0 = 0.01$. For each material, three numerical simulations were conducted considering distinct values of thickness $t = \{0.7, 0.8, 0.9\}$, corresponding to the limits of applicability of the proposed methodology. The resulting punch force–displacement curves for each material and thickness are presented in Figure 21a. In this graph, it is evident that materials with the same Young's modulus and identical thickness exhibit a similar punch force relationship in the elastic regime.

Table 8. Swift parameters and Young's modulus of virtual materials *VM4* and *VM5*.

	Swift Parameters			Young's Modulus
Material	K	ε_0	n	E (GPa)
VM4	600	0.0001	0.05	210
VM5	600	0.01	0.35	

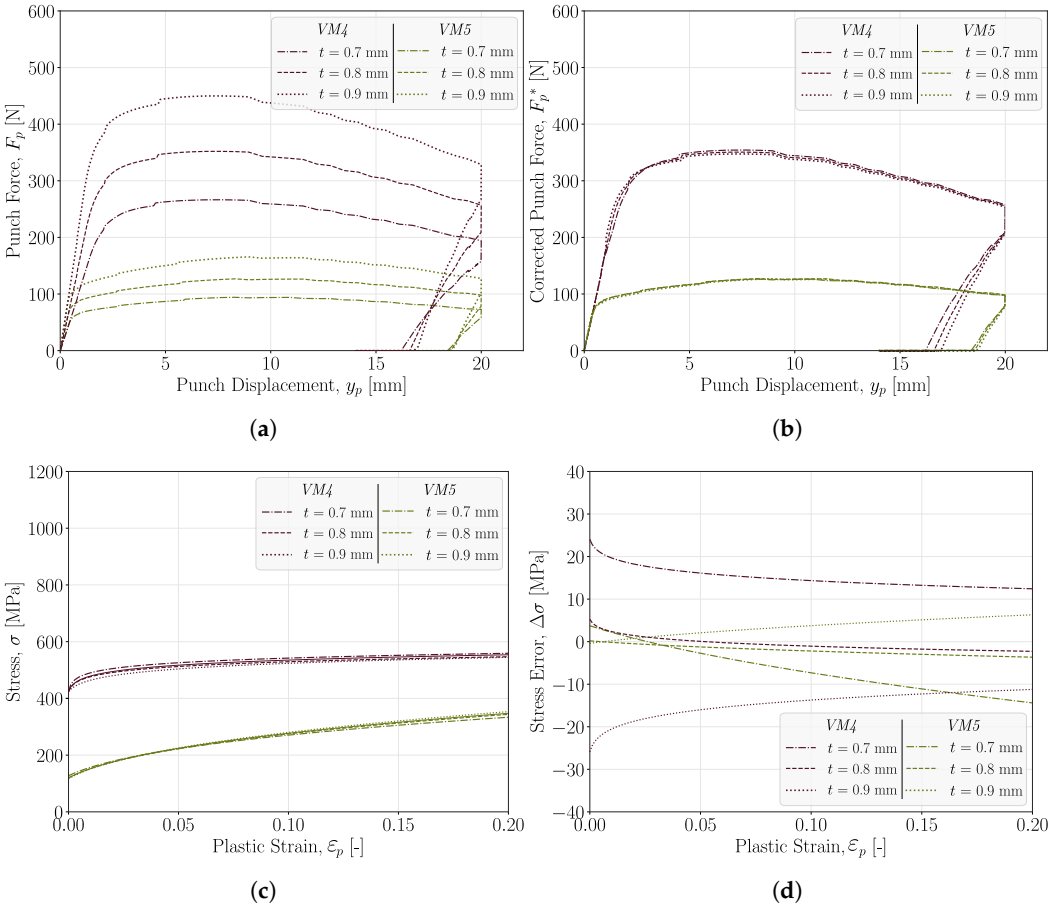

Figure 21. Influence of material thickness for *VM4* and *VM5* on (**a**) punch force–displacement curve, (**b**) corrected punch displacement curve, (**c**) true stress–strain curves predicted by the trained LSTM, and (**d**) stress error.

The corrected punch force–displacement curves for these materials are presented in Figure 21b. Applying Equation (18), two sets of parameters were considered: $n = 1$ and $\varepsilon_0 = 0$ for the elastic part, and the parameters $n = 0.15$ and $\varepsilon = 0.001$ for the plastic component of the curve. It is evident that even when assuming average parameter values,

the curves for thicknesses of 0.7 and 0.9 mm tend to closely align with the curve for the nominal thickness, $t_{nom} = 0.8$ mm, in both the elastic and plastic zones.

The true stress–strain curves corresponding to parameters predicted by the trained ML model, utilizing the corrected punch displacement curves for each case, are presented in Figure 21c. Upon comparison with the target curve, it is evident that, as expected, the predictions for cases where the material thickness is equal to the nominal thickness are very accurate, with the curves coinciding with the target. For these cases, the stress error, $\Delta\sigma$, is approximately 0 as represented in Figure 21d. On the other hand, for thicknesses different from the nominal thickness, there is an observable increase in prediction errors. The resulting stress–strain curves deviate slightly from the target curve, leading to higher stress errors. Nevertheless, these errors remain below 30 MPa for the cases under analysis, which can be considered admissible. It is important to note that this methodology is designed to be applied to small variations in thickness, and the specified thickness range of ± 0.1 mm was intentionally overestimated. In reality, variations around the nominal thickness are not expected to be of this order of magnitude. Therefore, the consideration of intermediate parameters for n and ε_0 results in an acceptable solution with stress errors lower than 30 MPa.

5.3. Experimental Results

After validating the two implemented ML models, this section focuses on evaluating their performance using experimental three-point bending results of the studied dual-phase steels (DP500, DP600, and DP780). The experimental punch force–displacement curves presented in Figure 5 were replaced by the corrected punch force–displacement curves, taking into consideration the measured thickness of each material (Table 1) and the average values of n and ε_0, set to 0.15 and 0.001, respectively.

For the first ML model that evaluates the elastic behavior and determines the Young's modulus of the material, twenty points were considered in the initial part of the curve between a punch displacement of 0 and 20 mm. The predicted Young's modulus for each material is summarized in Table 9. As expected, the Young's modulus of the three materials is closer to the reference modulus of steel, and the predicted values are also similar to those obtained using the analytical expression, Equation (12), with differences below 10 GPa. As the modulus of elasticity obtained falls within the limits allowed by the algorithm, i.e., [190 220], the ML model that predicts the Swift hardening parameters for steels can be applied.

Starting from the corrected experimental curve, 500 discrete points were selected across the curve to format the data for the application of the *ML model—plasticity*. The Swift hardening parameters (K, n, and ε_0) predicted by this model are summarized in Table 9. Additionally, they are compared with the Swift parameters obtained using the experimental tensile test and the optimization algorithm presented in Section 3.1. As is evident, the two methodologies provide different sets of hardening parameters, with the parameter ε_0 exhibiting the most significant differences. For DP780, the predicted ε_0 using the three-point bending test is 10 times higher than the one obtained by the tensile test.

Table 9. Comparison of Young's modulus predicted by the *ML model—elasticity* with the analytical approach (Equation (12)) and comparison of Swift parameters predicted by the *ML model—plasticity* with the parameters obtained from experimental tensile test curves.

	Young's Modulus		**Swift Parameters**					
	***E* (GPa)**		***K***		**ε_0**		***n***	
Material	**Analytical**	**Ml Elasticity**	**Tensile**	**3Point Bend**	**Tensile**	**3Point Bend**	**Tensile**	**3Point Bend**
DP500	192	191	865.32	835.56	0.0026	0.0035	0.1530	0.1421
DP600	208	209	1011.01	1063.21	0.0019	0.0039	0.1563	0.1805
DP780	196	194	1253.72	1281.27	0.0001	0.0010	0.1431	0.1559

To evaluate the impact of different parameter sets on the resulting true stress–strain ($\sigma - \varepsilon_p$) curves, the results for each material are systematized in Figures 22–24 for the DP500, DP600, and DP780, respectively. For each material, the left figure represents the corresponding true stress–strain curve considering the set of Swift law parameters obtained by the three-point test and the parameters obtained based on the experimental tensile test. The reference hardening curve obtained experimentally using the experimental tensile test is also represented. On the right side image, the stress error $\Delta\sigma$ for each Swift approximation is shown. In this case, the stress error is calculated as the difference in stress between each Swift curve and the experimental reference. A zero error indicates that for a given value of plastic strain, ε_p, the stress obtained from the Swift equation and the stress obtained experimentally are approximately equal. In the overall analysis, the Swift hardening law obtained by the three-point bending can approximate the stress–strain relation very well for all the considered materials, with an accuracy similar to the one obtained using traditional optimization algorithms based on the tensile test. The maximum stress error does not exceed 30 MPa for the considered range of plastic strain, a value that is in concordance with the analysis made in Section 5.2. Analyzing the results in detail for small values of plastic strain, specifically below $\varepsilon_p < 0.01$, it becomes clear that the Swift curve with parameters obtained by three-point bending tends to improve the characterization of the material's behavior. The error curves for $\varepsilon_p = 0$ tend to exhibit a significantly reduced error when considering the Swift curve with parameters obtained by three-point bending than the one obtained by the tensile test. Consequently, the estimated yield stress value tends to be more accurately characterized.

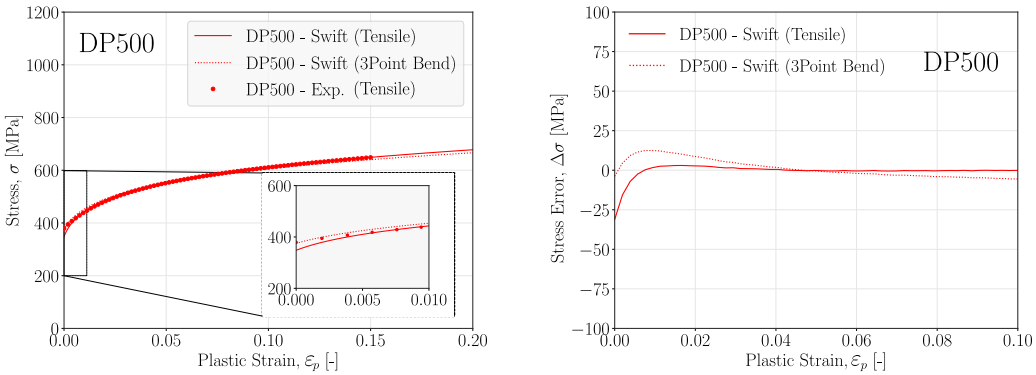

(**a**) (**b**)

Figure 22. Influence of Swift hardening parameters obtained based on the experimental tensile test and three-point bending Test on (**a**) true stress–strain curves and (**b**) respective stress error, $\Delta\sigma$, analysis for DP500 dual-phase steel.

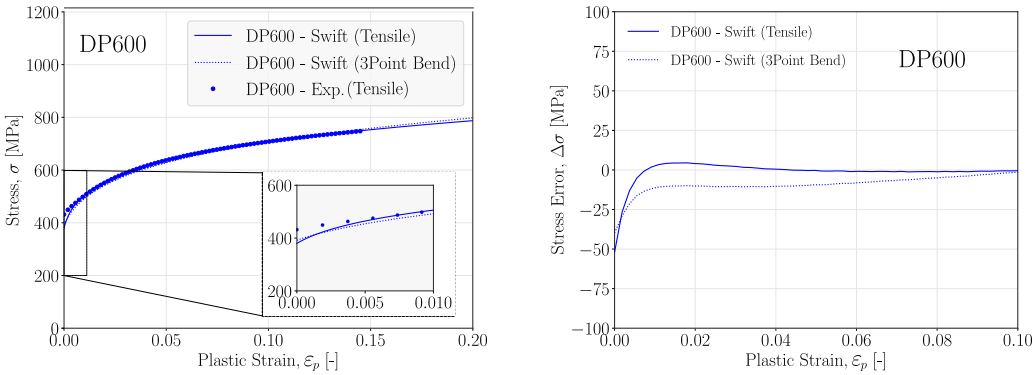

(**a**) (**b**)

Figure 23. Influence of Swift hardening parameters obtained based on experimental tensile test and three-point bending test on (**a**) true stress–strain curves and (**b**) respective stress error, $\Delta\sigma$, analysis for DP600 dual-phase steel.

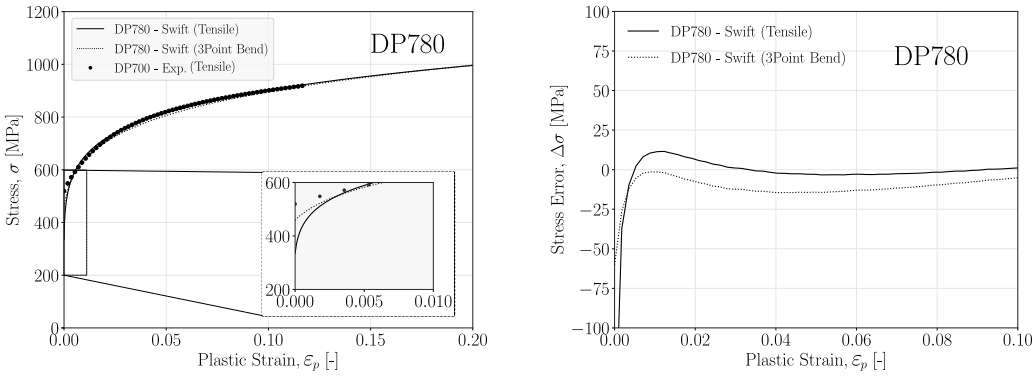

(**a**) (**b**)

Figure 24. Influence of Swift hardening parameters obtained based on experimental tensile test and three-point bending test on (**a**) true stress–strain curves and (**b**) respective stress error, $\Delta\sigma$, analysis for DP780 dual-phase steel.

6. Conclusions

This work provides a comprehensive study of the application of machine learning models (ML), specifically long short-term memory networks (LSTMs), to characterize material hardening behavior of sheet metal steels using the standard three-point bending tests. The sequential nature of the data obtained through this test, i.e., the force–displacement curve of the punch, led to the adoption of LSTMs instead of traditional feed-forward neural networks (FFNNs). The proposed methodology involves the use of two different ML models applied sequentially; namely, *ML model—elasticity* and *ML model—plasticity*. The first model is responsible for evaluating the elastic modulus of the tested material. If this Young's modulus falls within the range of 190 to 220 GPa, it indicates that the material in question possesses an elasticity characteristic of steel, and consequently, the second model, *ML model—plasticity*, can then be applied. This model is responsible for determining the Swift hardening parameters (K, n, ε_0) of steels. LSTMs have consistently demonstrated superior capabilities in capturing patterns in sequential data for both ML models, offering a more detailed and accurate representation of material behavior.

Regarding the first model (*ML model—elasticity*), which predicts the Young's modulus of the tested materials, it can be concluded that the developed LSTM network accurately estimates Young's modulus for materials with parameters in the range between 50 and 240 GPa. The performance of this model was evaluated for cases within an original data set and also for additional randomly generated materials, demonstrating its generalization capacity. The results indicate that the developed model adequately characterized the elastic modulus, demonstrating relative errors consistently below 3%.

For the second model (*ML Model—Plasticity*), which predicts material hardening parameters, a bidirectional LSTM architecture was employed, considering both the forward and backward punch force–displacement sequences. After implementing the LSTM and conducting hyperparameter tuning using the Bayesian optimization tuner, it was found that an LSTM network with 40 units proved to be efficient in simultaneously predicting the parameters K, n, and ε_0 in the respective ranges of [400, 1600], [0.0001, 0.01], and [0.05, 0.35]. The parameter ε_0 appears to have a lower prediction accuracy. However, the associated error does not significantly impact the predicted true stress–strain curves. On the other hand, the parameter K exhibited the most accurate prediction results, with relative errors below 7%. Nevertheless, it was also identified as the parameter that exerted the most significant influence on the final stress–strain relationship. In the worst-case scenarios, the trained model demonstrated a difference in the predicted stress value compared to the expected stress values of approximately 3%, which, in this context, can be considered acceptable. The evaluation of the influence of thickness on the three-point bending test results demonstrated the robustness of the methodology in dealing with variations around the nominal thickness. A new approach was considered to normalize the punch force,

resulting in a normalized value independent of the experimental material to be tested and characterized using this methodology. This approach assumed average parameter values for n and ε_0, and resulted in maintaining low stress errors, validating the methodology for small thickness variations around ± 0.1 mm.

Application of the developed ML models to experimental three-point bending tests using three grades of dual-phase steels (DP500, DP600, DP780) produced promising results. The *ML model—elasticity* accurately predicted Young's modulus values consistent with steel materials. Additionally, the *ML model—plasticity* successfully approximated Swift hardening parameters for dual-phase steels, offering a viable alternative to traditional optimization algorithms.

It is important to acknowledge the computational demands associated with the LSTM-based approach. The extended training time required for hyperparameter tuning in LSTMs poses a challenge, particularly as the dataset size grows. This computational demand is a trade-off for the improved predictive capabilities and the ability to capture temporal patterns offered by LSTMs compared to traditional ANNs .

In conclusion, this study establishes the efficacy of the LSTM-based ML models in accurately characterizing material behavior in three-point bending tests. The developed models exhibit strong predictive capabilities, a generalization to unseen materials, and demonstrate promising results when applied to experimental cases. These results position LSTM-based models as valuable tools for efficient hardening curve characterization for sheet metal forming applications.

Considering these conclusions, future work will involve expanding the methodology by exploring the use of pre-trained LSTM as the starting point of the new training phase to develop LSTMs for other thicknesses and materials, such as aluminum alloys. This approach is expected to offer advantages such as faster training times and improved performance by leveraging prior learning. Additionally, the methodology developed in this work will be expanded to include other mechanical tests, with a particular focus on those related to bending loadings. One potential application involves the bending–unbending test, which is fundamental for characterizing the kinematic hardening model of sheet metal materials. Finally, to enhance the robustness of this methodology, exploring the extension to physics-informed neural networks (PINNs) will be considered. The incorporation of a physics-based loss function can help limit variability and address outliers in the characterization process, especially in situations where a purely data-driven approach is used.

Author Contributions: Methodology, M.R.B., J.V.F. and A.D.S.; Software, D.J.C., R.L.A., A.D.S. and J.C.d.S.; Validation, D.J.C. and R.L.A.; Investigation, D.J.C. and M.R.B.; Writing—original draft, D.J.C.; Writing—review & editing, M.R.B., A.D.S., J.C.d.S. and J.V.F.; Visualization, D.J.C., M.R.B. and A.D.S.; Supervision, M.R.B., A.D.S., J.C.d.S. and J.V.F.; Funding acquisition, A.D.S. and J.V.F. All authors have read and agreed to the published version of the manuscript.

Funding: This work was supported by the project RealForm (reference 2022.02370.PTDC), funded by Portuguese Foundation for Science and Technology and by the Doctoral grant SFRH/BD/12657/2022 under the program POCH, co-financed by the European Social Fund (FSE) and Portuguese National Funds from MCTES.

Data Availability Statement: The data presented in this study are available on request from the corresponding author. The data are not publicly available due to privacy.

Acknowledgments: Authors highlight their appreciation and gratitude for the availability and fruitful discussions with J. Bessa Pacheco.

Conflicts of Interest: The authors declare no conflicts of interest.

Abbreviations

The following abbreviations are used in this manuscript:

AHSS	advanced high-strength steels
ANN	artificial neural network
FEA	finite element analysis
FEM	finite element modeling
FFNN	feed-forward neural network
SD	stress differential
DP	dual phase
DL	deep learning
CNN	convolutional neural network
LSTM	long short-term memory
RNN	recurrent neural network
RMSE	root mean square error
MSE	mean square error
MLP	multi-layer perceptron

References

1. Cao, J.; Banu, M. Opportunities and Challenges in Metal Forming for Lightweighting: Review and Future Work. *J. Manuf. Sci. Eng.* **2020**, *142*, 11. [CrossRef]
2. Wagoner, R.H. Sheet Springback. *Contin. Scale Simul. Eng. Mater. Fundam.–Microstruct.–Process Appl.* **2004**, 777–794. [CrossRef]
3. Prates, P.A.; Pereira, A.F.G. Recent Advances and Applications of Machine Learning in Metal Forming Processes. *Metals* **2022**, *12*, 1342. [CrossRef]
4. Pugliese, R.; Regondi, S.; Marini, R. Machine learning-based approach: Global trends, research directions, and regulatory standpoints. *Data Sci. Manag.* **2021**, *4*, 19–29. [CrossRef]
5. Liu, H.; Saksham, D.; Shen, M.; Chen, K.; Wu, V.; Wang, L. Industry 4.0 in Metal Forming Industry Towards Automotive Applications: A Review. *Int. J. Automot. Manuf. Mater.* **2022**, *1*, 1. [CrossRef]
6. Kim, H.; Chae, H.; Kwon, S.; Lee, S. Optimization of Deep Learning Parameters for Magneto-Impedance Sensor in Metal Detection and Classification. *Sensors* **2023**, *23*, 9259. [CrossRef]
7. Dib, M.A.; Oliveira, N.J.; Marques, A.E.; Oliveira, M.C.; Fernandes, J.V.; Ribeiro, B.M.; Prates, P.A. Single and ensemble classifiers for defect prediction in sheet metal forming under variability. *Neural Comput. Appl.* **2019**, *32*, 12335–12349. [CrossRef]
8. Tsai, S.Y.; Chang, J.Y. Parametric study and design of deep learning on leveling system for smart manufacturing. In Proceedings of the 2018 IEEE International Conference on Smart Manufacturing, Industrial & Logistics Engineering (SMILE), Hsinchu, Taiwan, 8–9 February 2018. [CrossRef]
9. Hamouche, E.; Loukaides, E.G. Classification and selection of sheet forming processes with machine learning. *Int. J. Comput. Integr. Manuf.* **2018**, *31*, 921–932. [CrossRef]
10. Lourenço, R.; Andrade-Campos, A.; Georgieva, P. The Use of Machine-Learning Techniques in Material Constitutive Modelling for Metal Forming Processes. *Metals* **2022**, *12*, 427. [CrossRef]
11. Jin, H.; Zhang, E.; Espinosa, H.D. Recent Advances and Applications of Machine Learning in Experimental Solid Mechanics: A Review. *Appl. Mech. Rev.* **2023**, *75*, 6. [CrossRef]
12. Palmieri, M.E.; Lorusso, V.D.; Tricarico, L. Robust Optimization and Kriging Metamodeling of Deep-Drawing Process to Obtain a Regulation Curve of Blank Holder Force. *Metals* **2021**, *11*, 319. [CrossRef]
13. Shamsuzzoha, A.; Kankaanpaa, T.; Nguyen, H.; Nguyen, H. Application of machine learning algorithm in the sheet metal industry: An exploratory case study. *Int. J. Comput. Integr. Manuf.* **2021**, *35*, 145–164. [CrossRef]
14. Li, W.; Zhang, L.C.; Wu, C.H.; Wang, Y.; Cui, Z.X.; Niu, C. A data-driven approach to RUL prediction of tools. *Adv. Manuf.* **2023** *11*. [CrossRef]
15. Uijl, N.D.; Carless, L. Advanced metal-forming technologies for automotive applications. In *Advanced Materials in Automotive Engineering*; Elsevier: Amsterdam, The Netherlands, 2012; pp. 28–56. [CrossRef]
16. Hovorun, T.P.; Berladir, K.V.; Pererva, V.I.; Rudenko, S.G.; Martynov, A.I. Modern materials for automotive industry. *J. Eng. Sci.* **2017**, *4*, f8–f18. [CrossRef]
17. Ghosh, M.; Ghosh, A.; Roy, A. Renewable and Sustainable Materials in Automotive Industry. In *Encyclopedia of Renewable and Sustainable Materials*; Elsevier: Amsterdam, The Netherlands, 2020; pp. 162–179. [CrossRef]
18. Hilditch, T.; de Souza, T.; Hodgson, P. Properties and automotive applications of advanced high-strength steels (AHSS). In *Welding and Joining of Advanced High Strength Steels (AHSS)*; Elsevier: Amsterdam, The Netherlands, 2015; pp. 9–28. [CrossRef]
19. Mendiguren, J.; Trujillo, J.J.; Cortés, F.; Galdos, L. An extended elastic law to represent non-linear elastic behaviour: Application in computational metal forming. *Int. J. Mech. Sci.* **2013**, *77*, 57–64. [CrossRef]

20. Joo, G.; Huh, H.; Kwon, J. Evaluation of rate-dependent hardening behaviors of AHSS sheets with novel tension and compression test devices. *J. Mater. Process. Technol.* **2019**, *270*, 365–379. [CrossRef]
21. Manopulo, N.; Barlat, F.; Hora, P. Isotropic to distortional hardening transition in metal plasticity. *Int. J. Solids Struct.* **2015**, *56–57*, 11–19. [CrossRef]
22. Chaboche, J. Constitutive equations for cyclic plasticity and cyclic viscoplasticity. *Int. J. Plast.* **1989**, *5*, 247–302. [CrossRef]
23. Alves, J.; Oliveira, M.; Menezes, L.; Cazacu, O. The role of tension-compression asymmetry of the plastic flow on ductility and damage accumulation of porous polycrystals. *Ciência Tecnol. Dos Mater.* **2017**, *29*, e234–e238. [CrossRef]
24. Yoshida, F.; Uemori, T. A model of large-strain cyclic plasticity describing the Bauschinger effect and workhardening stagnation. *Int. J. Plast.* **2002**, *18*, 661–686. [CrossRef]
25. Rauch, E.; Gracio, J.; Barlat, F. Work-hardening model for polycrystalline metals under strain reversal at large strains. *Acta Mater.* **2007**, *55*, 2939–2948. [CrossRef]
26. Versino, D.; Tonda, A.; Bronkhorst, C.A. Data driven modeling of plastic deformation. *Comput. Methods Appl. Mech. Eng.* **2017**, *318*, 981–1004. [CrossRef]
27. Aguir, H.; BelHadjSalah, H.; Hambli, R. Parameter identification of an elasto-plastic behaviour using artificial neural networks–genetic algorithm method. *Mater. Des.* **2011**, *32*, 48–53. [CrossRef]
28. Abbassi, F.; Belhadj, T.; Mistou, S.; Zghal, A. Parameter identification of a mechanical ductile damage using Artificial Neural Networks in sheet metal forming. *Mater. Des.* **2013**, *45*, 605–615. [CrossRef]
29. Schulte, R.; Karca, C.; Ostwald, R.; Menzel, A. Machine learning-assisted parameter identification for constitutive models based on concatenated loading path sequences. *Eur. J. Mech. A/Solids* **2023**, *98*, 104854. [CrossRef]
30. Marques, A.; Pereira, A.; Ribeiro, B.; Prates, P.A. On the Identification of Material Constitutive Model Parameters Using Machine Learning Algorithms. *Key Eng. Mater.* **2022**, *926*, 2146–2153. [CrossRef]
31. Ghaboussi, J.; Sidarta, D. New nested adaptive neural networks (NANN) for constitutive modeling. *Comput. Geotech.* **1998**, *22*, 29–52. [CrossRef]
32. Bock, F.E.; Aydin, R.C.; Cyron, C.J.; Huber, N.; Kalidindi, S.R.; Klusemann, B. A Review of the Application of Machine Learning and Data Mining Approaches in Continuum Materials Mechanics. *Front. Mater.* **2019**, *6* . [CrossRef]
33. Jang, D.P.; Fazily, P.; Yoon, J.W. Machine learning-based constitutive model for J2- plasticity. *Int. J. Plast.* **2021**, *138*, 102919. [CrossRef]
34. Zhang, A.; Mohr, D. Using neural networks to represent von Mises plasticity with isotropic hardening. *Int. J. Plast.* **2020**, *132*, 102732. [CrossRef]
35. Ibáñez, R.; Abisset-Chavanne, E.; González, D.; Duval, J.L.; Cueto, E.; Chinesta, F. Hybrid constitutive modeling: Data-driven learning of corrections to plasticity models. *Int. J. Mater. Form.* **2018**, *12*, 717–725. [CrossRef]
36. Huber, N.; Tsakmakis, C. A neural network tool for identifying the material parameters of a finite deformation viscoplasticity model with static recovery. *Comput. Methods Appl. Mech. Eng.* **2001**, *191*, 353–384. [CrossRef]
37. Ktari, Z.; Leitão, C.; Prates, P.A.; Khalfallah, A. Mechanical design of ring tensile specimen via surrogate modelling for inverse material parameter identification. *Mech. Mater.* **2021**, *153*, 103673. [CrossRef]
38. Yao, D.; Duan, Y.-c.; Li, M.-y.; Guan, Y.-p. Hybrid identification method of coupled viscoplastic-damage constitutive parameters based on BP neural network and genetic algorithm. *Eng. Fract. Mech.* **2021**, *257*, 108027. [CrossRef]
39. Morand, L.; Helm, D. A mixture of experts approach to handle ambiguities in parameter identification problems in material modeling. *Comput. Mater. Sci.* **2019**, *167*, 85–91. [CrossRef]
40. Heider, Y.; Wang, K.; Sun, W. SO(3)-invariance of informed-graph-based deep neural network for anisotropic elastoplastic materials. *Comput. Methods Appl. Mech. Eng.* **2020**, *363*, 112875. [CrossRef]
41. Abueidda, D.W.; Koric, S.; Sobh, N.A.; Sehitoglu, H. Deep learning for plasticity and thermo-viscoplasticity. *Int. J. Plast.* **2021**, *136*, 102852. [CrossRef]
42. Ghavamian, F.; Simone, A. Accelerating multiscale finite element simulations of history-dependent materials using a recurrent neural network. *Comput. Methods Appl. Mech. Eng.* **2019**, *357*, 112594. [CrossRef]
43. Gorji, M.B.; Mozaffar, M.; Heidenreich, J.N.; Cao, J.; Mohr, D. On the potential of recurrent neural networks for modeling path dependent plasticity. *J. Mech. Phys. Solids* **2020**, *143*, 103972. [CrossRef]
44. Mozaffar, M.; Bostanabad, R.; Chen, W.; Ehmann, K.; Cao, J.; Bessa, M.A. Deep learning predicts path-dependent plasticity. *Proc. Natl. Acad. Sci.* **2019**, *116*, 26414–26420. [CrossRef]
45. Guo, Z.; Bai, R.; Lei, Z.; Jiang, H.; Liu, D.; Zou, J.; Yan, C. CPINet: Parameter identification of path-dependent constitutive model with automatic denoising based on CNN-LSTM. *Eur. J. Mech.-A/Solids* **2021**, *90*, 104327. [CrossRef]
46. Cruz, D.J.; Barbosa, M.R.; Santos, A.D.; Miranda, S.S.; Amaral, R.L. Application of Machine Learning to Bending Processes and Material Identification. *Metals* **2021**, *11*, 1418. [CrossRef]
47. Schmidt, R.M. Recurrent Neural Networks (RNNs): A gentle Introduction and Overview. *arXiv* **2019**, arXiv:1912.05911.
48. Sherstinsky, A. Fundamentals of Recurrent Neural Network (RNN) and Long Short-Term Memory (LSTM) network. *Phys. D Nonlinear Phenom.* **2020**, *404*, 132306. [CrossRef]
49. Hochreiter, S.; Schmidhuber, J. Long Short-Term Memory. *Neural Comput.* **1997**, *9*, 1735–1780. [CrossRef] [PubMed]
50. Sutskever, I.; Vinyals, O.; Le, Q.V. Sequence to sequence learning with neural networks. *Adv. Neural Inf. Process. Syst.* **2014**, *27*, 3104–3112.

51. Graves, A.; Mohamed, A.r.; Hinton, G. Speech recognition with deep recurrent neural networks. In Proceedings of the 2013 IEEE International Conference on Acoustics, Speech and Signal Processing, Vancouver, British, 26–31 May 2013; pp. 6645–6649.
52. Amodei, D.; Ananthanarayanan, S.; Anubhai, R.; Bai, J.; Battenberg, E.; Case, C.; Casper, J.; Catanzaro, B.; Cheng, Q.; Chen, G.; et al. Deep speech 2: End-to-end speech recognition in English and Mandarin. *arXiv* **2016**, arXiv:1512.02595.
53. Chan, W.; Jaitly, N.; Le, Q.; Vinyals, O. Listen, attend and spell. In Proceedings of the 2016 IEEE International Conference on Acoustics, Speech and Signal Processing (ICASSP), Shanghai, China, 20–25 March 2016; pp. 2620–2624.
54. Zhang, A.; Lipton, Z.C.; Li, M.; Smola, A.J. *Dive into Deep Learning*; Cambridge University Press: Cambridge, UK, 2021. [CrossRef]
55. DiPietro, R.; Hager, G.D. Deep learning: RNNs and LSTM. In *Handbook of Medical Image Computing and Computer Assisted Intervention*; Elsevier: Amsterdam, The Netherlands, 2020; pp. 503–519. [CrossRef]
56. *ASTM E8*; E8M-16ae1—Standard Test Methods for Tension Testing of Metallic Materials. American Society for Testing and Materials: West Conshohocken, PA, USA, 2016.
57. Lagarias, J.C.; Reeds, J.A.; Wright, M.H.; Wright, P.E. Convergence Properties of the Nelder–Mead Simplex Method in Low Dimensions. *SIAM J. Optim.* **1998**, *9*, 112–147. [CrossRef]
58. *ASTM E290*; Standard Test Methods For Bend Testing Of Material For Ductility. ASTM International: West Conshohocken, PA, USA, 2014.
59. Sofuoğlu, M.A.; Gürgen, S.; Çakır, F.H.; Orak, S. Springback Behavior of AA6082T6 Tubes in Three-point Bending Operation. *Procedia Eng.* **2017**, *182*, 658–664. [CrossRef]
60. Raabe, D.; Roters, F.; Barlat, F.; Chen, L.Q. *Continuum Scale Simulation of Engineering Materials: Fundamentals, Microstructures, Process Applications*; Wiley-VCH: Weinheim, Germany, 2004.
61. Wagner, L.; Larour, P.; Dolzer, D.; Leomann, F.; Suppan, C. Experimental issues in the instrumented 3 point bending VDA238-100 test. *IOP Conf. Ser. Mater. Sci. Eng.* **2020**, *967*, 012079. [CrossRef]
62. Naseem, S.; Perdahcıoğlu, E.S.; Geijselaers, H. J. M.van den Boogaard, A. A New in-Plane Bending Test to Determine Flow Curves for Materials with Low Uniform Elongation. *Exp. Mech.* **2020**, *60*, 1225–1238. [CrossRef]
63. Mujika, F. Three-Point Bending Test Procedure: Rectangular Cross Section. 2020. Available online: https://www.researchgate.net/publication/344267126_THREE-POINT_BENDING_TEST_PROCEDURE_RECTANGULAR_CROSS_SECTION?channel=doi&linkId=5f61f63d4585154dbbd57fe4&showFulltext=true (accessed on 1 December 2023).
64. Kim, Y.J.; Lee, C.H.; Kim, J.H.; Lim, J.H. Numerical modeling of shape memory alloy plates considering tension/compression asymmetry and its verification under pure bending. *Int. J. Solids Struct* **2018**, *136–137*, 77–88. [CrossRef]
65. Badr, O.M.; Rolfe, B.; Zhang, P.; Weiss, M. Applying a new constitutive model to analyse the springback behaviour of titanium in bending and roll forming. *Int. J. Mech. Sci.* **2017**, *128–129*, 389–400. [CrossRef]
66. Capilla, G.; Hamasaki, H.; Yoshida, F. Determination of uniaxial large-strain workhardening of high-strength steel sheets from in-plane stretch-bending testing. *J. Mater. Process. Technol* **2017**, *243*, 152–169. [CrossRef]
67. Nádai, Á.; Wahl, A.M.; Bingham, E.C. iPlasticity, A Mechanics of the Plastic State of Matter/i. *J. Rheol.* **1931**, *2*, 455–456. [CrossRef]
68. Mujika, F. On the effect of shear and local deformation in three-point bending tests. *Polym. Test.* **2007**, *26*, 869–877. [CrossRef]
69. Dassault Systèmes. *Abaqus Analysis User's Manual*; Version 2021; Dassault Systèmes: Providence, RI, USA, 2021.
70. Ferreira, B. Integração de Metodologias de Análise do Processo de Quinagem. Master's Thesis, Faculdade de Engenharia da Universidade do Porto, Porto, Portugal, 2015.
71. Deng, N.; Korkolis, Y.P. Elastic anisotropy of dual-phase steels with varying martensite content. *Int. J. Solids Struct.* **2018**, *141–142*, 264–278. [CrossRef]
72. de Souza, T.; Rolfe, B. Multivariate modelling of variability in sheet metal forming. *J. Mater. Process. Technol.* **2008**, *203*, 1–12. [CrossRef]
73. Marciniak, Z.; Duncan, J.; Hu, S. (Eds.) 6—Bending of sheet. In *Mechanics of Sheet Metal Forming*, 2nd ed.; Butterworth-Heinemann: Oxford, UK, 2002; pp. 82–107. [CrossRef]
74. Mentink, R.; Lutters, D.; Streppel, A.; Kals, H. Determining material properties of sheet metal on a press brake. *J. Mater. Process. Technol.* **2003**, *141*, 143–154. [CrossRef]
75. Zhai, X.; Zhang, F.; Zhao, H.; Li, C.; Xu, Z.; Hao, X.; Zhu, Z.; Xu, X. Research on the Effects of Friction Coefficient on Three-Point Bending by Finite Element Analysis. *J. Comput. Theor. Nanosci.* **2015**, *12*, 5139–5143. [CrossRef]
76. Chollet, F.; Keras. 2015 Available online: https://keras.io (accessed on 1 December 2023).
77. Snoek, J.; Larochelle, H.; Adams, R.P. Practical Bayesian Optimization of Machine Learning Algorithms. In *Advances in Neural Information Processing Systems*; Curran Associates Inc.: Red Hook, NY, USA, 2012; pp. 2951–2959.